Department of Precision and Microsystems Engineering

A Discontinuity-Enriched Finite Element Method for Dynamic Fracture in Brittle Materials

Yuheng Yan

Report no : 2021.019
Coach : Dr. Alejandro M. Aragón
Specialisation : Engineering Mechanics
Type of report : Master of Science Thesis
Date : 26 March 2021

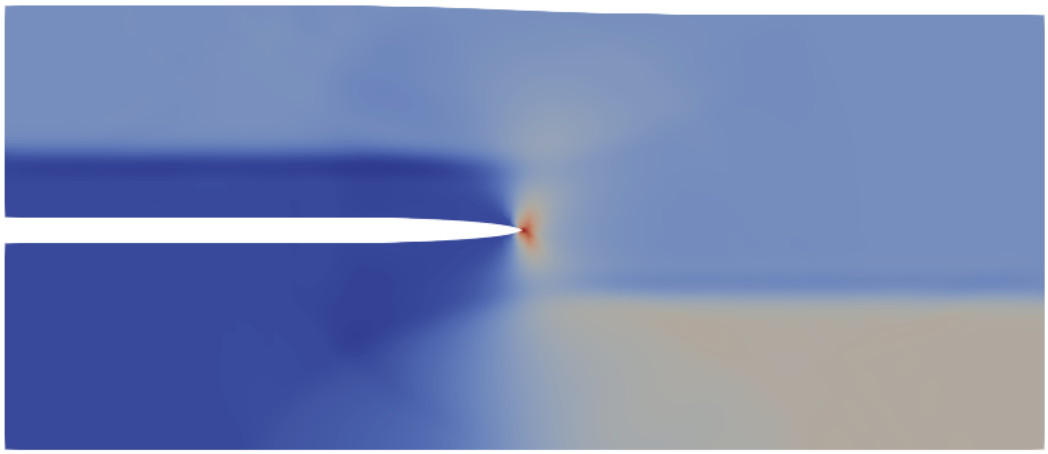

TU Delft Delft University of Technology

Challenge the future

A Discontinuity-Enriched Finite Element Method for Dynamic Fracture in Brittle Materials

by

Yuheng YAN

to obtain the degree of Master of Science
in Mechanical Engineering
at the Delft University of Technology,
to be defended on Friday March 26th, 2021.

Student number: 4810074

Thesis committee:	Dr. A. M. Aragón (Chair)	TU Delft, 3ME, supervisor
	Dr.ir. R. A. J. van Ostayen	TU Delft, 3ME
	J. Zhang, M.Sc.	TU Delft, 3ME
	Dr. C. L. Walters	TU Delft, 3ME

An electronic version of this dissertation is available at
http://repository.tudelft.nl/.

Acknowledgements

The journey of my master of science's thesis work finally comes to the end. The experience on the project "A Discontinuity-enriched Finite Element Method for Dynamic Fracture in Brittle Materials" is precious. During this period, I learned valuable skills and knowledge while overcoming difficulties and challenges.

First of all, I would like to sincerely thank my supervisor Dr. Alejandro Aragón for the nice suggestions when I had difficulties. He also helped me catching my schedule when I had unexpected time delays with my project. His critical attitude and outstanding research skills have shown me the characteristics an excellent researcher should have. Also, I would like to thank my PhD senior Jian Zhang, who gave me hands on coding. Despite his busy schedule, he spent a lot of time telling me how to properly code with *Hybrida*. Besides, the collaborations with my peers in *Hybrida* group was nice and I will never forget the time working with them.

The two year and a half study at Delft University of Technology (TU Delft) is memorable. I was immersed in the international environment and learned interdisciplinary subjects related to mechanics and mechatronics. I met lots of friends. Thanks to the friends from Department of Precision and Microsystems Engineering, with whom I had nice time learning and discussing. I will remember friends from van Hasseltlaan forever, for the fun we had together playing games and cooking dishes. I am very glad to have Chenxi and Chenyang as my good friends since they are such virtuous people that are always friendly and gentle.

Studying at TU Delft is not easy. I would like to give my great gratitude to my parents for their love and support. The video chats every weekends always make me relaxed and refreshed. Thanks to my girlfriend Xinrui, a kind girl who encouraged me a lot in the difficult time. I believe she will soon overcome difficulties of her project. Lastly, thanks to Chenxi for looking after me when I was seriously injured while riding bike.

Yuheng Yan
Delft, March 2021

Abstract

The computational modeling of crack propagation is important in aerospace and automotive industries because cracks play a significant role in structural failure. In comparison with the quasi-static case, inertial effects are significant in dynamic crack propagation. The classical numerical tool for modeling dynamic crack propagation is the standard finite element method (FEM). However, the method suffers from problem of mesh-dependency. Enriched finite element procedures such as the eXtended/Generalized finite element method (X/GFEM) are able to solve this issue by adding enriched degrees of freedom (DOFs) to nodes of the original mesh, thereby providing full decoupling between the mesh and cracks. Yet, X/GFEM suffers from other issues that are inherent to the formulation such as the need for more complicated methods for applying non-zero Dirichlet boundary condition, and an intricate computer implementation.

In the thesis, the Discontinuity-Enriched Finite Element Method (DE-FEM) is used to simulate dynamic crack propagation as an alternative to X/GFEM. DE-FEM also decouples cracks from the background mesh while solving X/GFEM's aforementioned issues. This is achieved by adding enriched DOFs along cracks. Prescribing non-zero essential boundary conditions is as straightforward as in standard FEM. Moreover, DE-FEM's enrichment strategy provides simplicity on crack propagation, as the crack tip node can be transformed into a crack segment node directly with little effort. Also, fewer enriched DOFs than in X/GFEM are appended while advancing cracks. In the numerical examples of either stationary crack with dynamic loading or dynamically propagating cracks, DE-FEM is able to reproduce analytical and/or experimental results. Both Bathe's time integration method and the classical Newmark constant average acceleration method are applied and compared. Results show DE-FEM is a suitable candidate to solve dynamic fracture problems.

Contents

1

Introduction

Fracture in brittle solids is of interest in several industries, including aerospace [1], civil engineering [2], biomechanics [3], and automotive [4]. Fracture raises concerns of both safety and cost in engineering practice [5]. Therefore, understanding fracture behavior, and particularly crack propagation, is of great importance in engineering. Experiments could be conducted to understand crack propagation [6, 7] but they are time-consuming and easily affected by unwanted conditions like temperature and humidity. Numerical methods could get rid of these problems. In numerical analysis, crack propagation can be modeled either as quasi-static or dynamic. While the material inertia is neglected in quasi-static propagation, dynamic crack propagation is concerned with phenomena for which the role of it becomes significant [8], such as fast crack growth or rapid time loading [9]. These dynamic cases are widely encountered in practice so this thesis is going to look at numerical simulations of dynamic crack propagation.

The classical way to simulate dynamic crack propagation is to use the standard finite element method (Std. FEM) where cracks align with element edges [10]. In order to match mesh with crack geometry, remeshing is needed for each propagation step. Examples of this *remeshing technique* are works of Atluri *et al.* [11] and Swenson *et al* [12]. However, this technique is computationally expensive because new mesh should be regenerated at each finite element analysis. This problem becomes more serious if small time step is used or the crack advances over a large domain of mesh.

The eXtended/Generalized finite element method (X/GFEM) was proposed to avoid remeshing by decoupling the representation of cracks and the background mesh [13]. Early works of X/GFEM on dynamic crack propagation were from Belytschko *et al.* [14] and Duarte *et al* [15]. Later, Belytschko *et al.* [16] proposed a framework for dynamic crack propagation in which stress intensity factors (SIFs) were taken as additional degrees of freedom (DOFs) and evaluated directly by the discrete momentum equation. Then Song *et al.* [17] proposed a phantom node method where the crack is described by superimposed elements and phantom nodes. However, the expression of interaction integral, which is widely applied in quasi-static crack problems to evaluate SIFs [13], still remained unknown for dynamic crack. Therefore, based on work of Attigui [18], Réthoré *et al.* [19] proposed a path-independent dynamic interaction integral to compute SIFs. As the functions that span the finite element space change as crack advances, in the same paper they also proposed a mapping scheme in order to relate DOFs before and after the instance of crack propagation. Nevertheless, dynamic SIFs obtained by X/GFEM shows oscillations no matter the crack is stationary or propagating [19–21]. Many attempts were made to understand and solve this issue [22–24] but none of them completely removed the oscillations. Moreover, X/GFEM has intrinsic drawbacks due to its formulation. The non-cut elements that share enriched DOFs, namely *blending elements*, lose their accuracy [25]. Also as the enriched nodes are added to the background mesh nodes, the original DOFs lose their physical meanings, and the imposition of Dirichlet boundary conditions is not as straightforward as Std. FEM.

The Discontinuity-enriched finite element method (DE-FEM) was proposed to tackle the intrinsic drawbacks of X/GFEM while preserving the advantage of X/GFEM on decoupling representation of cracks and the background mesh [26–28]. The enriched nodes are created at intersections between cracks and the background element edges, and the corresponding enrichment functions are established with *Lagrange* shape functions of integration elements. The enrichment functions decrease to zero at background element nodes by construction, and consequently there is no issue of blending elements as in X/GFEM. Furthermore, DOFs

associated to these nodes retain their physical meanings. By virtue of this property, Dirichlet boundary condition can be imposed in a strong form.

As DE-FEM has the aforementioned intrinsic advantages, this thesis is going to apply it to solve dynamic crack propagation problems and study its behavior and functionality. We show that propagating cracks in the framework of DE-FEM is straightforward by simply adding the enriched nodes along the propagated crack segments. Also the transition of crack tip node to crack segment node is straightforward due to the enrichment strategy. All the results are shown by popular benchmark examples of stationary crack with dynamic loading as well as dynamic crack propagation. By DE-FEM, analytical and/or experimental results are reproduced. Furthermore, both Bathe's time integration method and Newmark constant average acceleration method are implemented compared, and the first method shows its capability on removing oscillations of SIFs for stationary crack with dynamic loading problems.

2

A Discontinuity-enriched Finite Element Method for Dynamic Fracture in Brittle Materials

2.1. Problem Description

In this chapter we look at dynamic fracture mechanical problems in a time interval $\Gamma = [0, T]$. Let us consider a continuous body Ω with a crack, which is illustrated in Figure 2.1. The domain is enclosed by its boundary $\partial\Omega$ composed of the sets $\partial\Omega_D$, $\partial\Omega_N$, Γ^+, and Γ^-, such that $\partial\Omega = \partial\Omega_D \cup \partial\Omega_N \cup \Gamma^+ \cup \Gamma^-$. Prescribed displacement $\bar{\boldsymbol{u}}(\boldsymbol{x}, t)$ is imposed on $\partial\Omega_D$ and prescribed traction $\bar{\boldsymbol{t}}(\boldsymbol{x}, t)$ is imposed on $\partial\Omega_N$. Two crack surfaces Γ^+, Γ^- are assumed to be traction free. The structure is assigned with an isotropic and homogeneous brittle material, with Young's modulus E, Poisson's ratio ν, and density ρ. Let $\boldsymbol{u}(\boldsymbol{x}, t) : \Omega \times \Gamma \to \mathbb{R}^2$ be displacement field. The dynamic equilibrium equation of this continuous problem is

$$\nabla \cdot \boldsymbol{\sigma} + \boldsymbol{b} = \rho \ddot{\boldsymbol{u}}, \tag{2.1}$$

where $\boldsymbol{\sigma}(\boldsymbol{x}, t) : \Omega \times \Gamma \to \mathbb{R}^2 \times \mathbb{R}^2$, $\boldsymbol{b}(\boldsymbol{x}, t) : \Omega \times \Gamma \to \mathbb{R}^2$ and $\ddot{\boldsymbol{u}}(\boldsymbol{x}, t) = \frac{\partial^2 \boldsymbol{u}}{\partial t^2} : \Omega \times \Gamma \to \mathbb{R}^2$ are Cauchy stress tensor, body force, and acceleration, respectively. Boundary conditions are expressed as

$$\begin{aligned} \boldsymbol{u} &= \bar{\boldsymbol{u}}, && \text{on } \partial\Omega_D, \\ \boldsymbol{\sigma} \cdot \boldsymbol{n} &= \bar{\boldsymbol{t}}, && \text{on } \partial\Omega_N, \\ \boldsymbol{\sigma} \cdot \boldsymbol{n} &= \boldsymbol{0}, && \text{on } \Gamma^+ \text{ and } \Gamma^-, \end{aligned} \tag{2.2}$$

where $\boldsymbol{n}$ is vector normal to the domain boundary $\partial\Omega$. The third equation of Equation (2.1) reflects the traction free condition on crack surfaces. As we are solving an initial-boundary value problem, the initial condition is defined as

$$\begin{aligned} \boldsymbol{u}(\boldsymbol{x}, 0) &= \boldsymbol{u_0}(\boldsymbol{x}), \\ \dot{\boldsymbol{u}}(\boldsymbol{x}, 0) &= \dot{\boldsymbol{u}}_{\boldsymbol{0}}(\boldsymbol{x}), \end{aligned} \tag{2.3}$$

where $\dot{\boldsymbol{u}}(\boldsymbol{x}, t) = \frac{\partial \boldsymbol{u}}{\partial t}$ is velocity. In this study, we consider problem with small deformation so linearized strain tensor is written as $\boldsymbol{\epsilon} = \frac{1}{2}(\nabla \boldsymbol{u} + \nabla^T \boldsymbol{u})$. Similarly, we also assume a linear constitutive relation (Hook's law) $\boldsymbol{\sigma} = \boldsymbol{C}\boldsymbol{\epsilon}$, where $\boldsymbol{C}$ is fourth-order constitutive tensor.

Equation (2.1) to Equation (2.3) are also called strong form of equilibrium. They describe equilibrium of system pointwise for all $(\boldsymbol{x}, t) \in \Omega \times \Gamma$. With these equations, the problem is well defined. Let $\boldsymbol{\omega} \in \boldsymbol{W}$ be an arbitrary weight function from functional space $\boldsymbol{W}$ which satisfies

$$\boldsymbol{W} = \left\{ \boldsymbol{\omega} : \boldsymbol{\omega}(\boldsymbol{x}, t) \in \mathbb{R}^2 \forall (\boldsymbol{x}, t) \in \Omega \times \Gamma, \boldsymbol{\omega}|_{\partial\Omega_D} = \boldsymbol{0} \right\}. \tag{2.4}$$

The weak form is: find $\boldsymbol{u}(\boldsymbol{x}, t) \in \boldsymbol{U}$ such that $\forall \boldsymbol{w} \in \boldsymbol{W}$

$$\int_\Omega \rho \boldsymbol{\omega} : \ddot{\boldsymbol{u}} \mathrm{d}\Omega + \int_\Omega \nabla \boldsymbol{\omega} : \boldsymbol{\sigma} \mathrm{d}\Omega = \int_\Omega \boldsymbol{\omega} \cdot \boldsymbol{b} \mathrm{d}\Omega + \int_{\partial\Omega_N} \boldsymbol{\omega} \cdot \bar{\boldsymbol{t}} \mathrm{d}\partial\Omega, \tag{2.5}$$

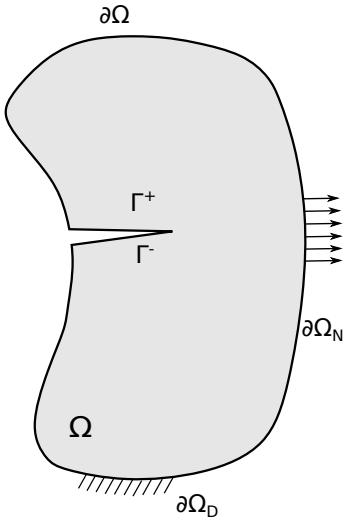

Figure 2.1: Continuous domain Ω with a crack. Crack surfaces Γ^+ and Γ^- are traction-free. Prescribed displacements and tractions are applied on $\partial\Omega_D$ and $\partial\Omega_N$, respectively.

where space $\boldsymbol{U}$ is

$$\boldsymbol{U} = \left\{ \boldsymbol{u} : \boldsymbol{u}(\boldsymbol{x}, t) \in \mathbb{R}^2 \forall (\boldsymbol{x}, t) \in \Omega \times \Gamma, \boldsymbol{u}(\boldsymbol{x}, t)|_{\partial\Omega_D} = \bar{\boldsymbol{u}}, u_i \in \boldsymbol{H}^1(\Omega), i = 1,2 \right\}. \tag{2.6}$$

2.2. Discrete Formulation with the Discontinuity-enriched Finite Element Method

In order to find a suitable solution to the aforementioned problem by FEM, the Galerkin projection is applied to the weak form of equilibrium (2.5). This method requires finite dimensional function spaces to approximate displacement field $\boldsymbol{u}$ and weight function $\boldsymbol{\omega}$. The approximated displacement is denoted as $\boldsymbol{u}^h$ to be distinguished with real displacement $\boldsymbol{u}$, similarly for $\boldsymbol{\omega}^h$.

The discontinuity-enriched finite element method (DE-FEM) was proposed by Aragón *et al.* [26] to model problems with weak and strong discontinuities, which means problems with solutions that are C^0- and C^1-continuous, respectively. The displacement field of DE-FEM takes the form

$$\boldsymbol{u^h} = \underbrace{\sum_{i \in \iota_h} \boldsymbol{N}_i(\boldsymbol{x}) \boldsymbol{U}_i(t)}_{\text{std. FEM}} + \underbrace{\sum_{i \in \iota_w} \boldsymbol{\psi}_i(\boldsymbol{x}) \boldsymbol{\alpha}_i(t)}_{\text{weak}} + \underbrace{\sum_{i \in \iota_s} \boldsymbol{\chi}_i(\boldsymbol{x}) \boldsymbol{\beta}_i(t)}_{\text{strong}}. \tag{2.7}$$

Equation (2.7) consists of three terms with different functions. The first term is the same as in the standard finite element method. Therefore, the standard FEM space is enriched. ι_h is the set containing all standard nodes. $\boldsymbol{N}_i(\boldsymbol{x})$ and $\boldsymbol{U}_i(t)$ are standard shape functions and degrees of freedom (DOFs), respectively. The second term enables DE-FEM to model weak discontinuities, in which ι_w is the node set of weak discontinuity and $\boldsymbol{\alpha}_i$ is the corresponding enriched DOFs. The weak enrichment $\boldsymbol{\psi}_i(\boldsymbol{x})$ is constructed by Soghrati *et al.* [29] in the context of Interface-enriched Generalized Finite Element Method (IGFEM). The last term is for modeling strong discontinuities. Similar to the weak term, the enrichment function $\boldsymbol{\chi}_i(\boldsymbol{x})$ reproduces the kinematics of a strong discontinuity. Set ι_s is the node set for all strong nodes and $\boldsymbol{\beta}_i$ is strong DOFs. Both strong and weak enrichments decrease to zero at element nodes.

DE-FEM was originally proposed for fracture mechanics problems. The crack tip is enriched with only a weak node because at the tip location there is no displacement jump (strong discontinuity). The rest of the crack is endowed with both strong and weak nodes, as introduced in Equation (2.7).

Starting from the weak form (2.5) and following Galerkin procedure, we can reach the discrete governing equation of the problem in Section 2.1

$$\boldsymbol{M}\ddot{\boldsymbol{u}} + \boldsymbol{K}\boldsymbol{u} = \boldsymbol{F}, \tag{2.8}$$

where $\boldsymbol{M}$,$\boldsymbol{K}$ and $\boldsymbol{F}$ are the mass matrix, the stiffness matrix, and the force vector. Let $\boldsymbol{\phi}$ be the matrix that

contains all non -zero standard shape functions and enrichment functions on a specific element e

$$\boldsymbol{\phi} = \begin{bmatrix} N_1 & 0 & \dots & \psi_1 & 0 & \dots & \chi_1 & 0 & \dots \\ 0 & N_1 & \dots & 0 & \psi_1 & \dots & 0 & \chi_1 & \dots \end{bmatrix}, \tag{2.9}$$

and $\boldsymbol{B}$ be the matrix of derivatives of these shape and enrichment functions with respect to Cartesien coordinates x and y

$$\boldsymbol{B} = \begin{bmatrix} \frac{\partial N_1}{\partial x} & 0 & \dots & \frac{\partial \psi_1}{\partial x} & 0 & \dots & \frac{\partial \chi_1}{\partial x} & 0 & \dots \\ 0 & \frac{\partial N_1}{\partial y} & \dots & 0 & \frac{\partial \psi_1}{\partial y} & \dots & 0 & \frac{\partial \chi_1}{\partial y} & \dots \\ \frac{\partial N_1}{\partial y} & \frac{\partial N_1}{\partial x} & \dots & \frac{\partial \psi_1}{\partial y} & \frac{\partial \psi_1}{\partial x} & \dots & \frac{\partial \chi_1}{\partial y} & \frac{\partial \chi_1}{\partial x} & \dots \end{bmatrix}. \tag{2.10}$$

Therefore, the mass matrix $\boldsymbol{m}_e$, stiffness matrix $\boldsymbol{k}_e$, and force vector $\boldsymbol{f}_e$ of this element is constructed by

$$\boldsymbol{m}_e = \int_e \rho \boldsymbol{\phi}^\mathsf{T} \boldsymbol{\phi} \mathrm{d}e, \qquad \boldsymbol{k}_e = \int_e \boldsymbol{B}^\mathsf{T} \boldsymbol{D} \boldsymbol{B} \mathrm{d}e, \qquad \boldsymbol{f}_e = \int_e \boldsymbol{\phi}^\mathsf{T} \boldsymbol{b} \mathrm{d}e + \int_{\partial e} \boldsymbol{\phi}^\mathsf{T} \bar{\boldsymbol{t}} \mathrm{d}\partial e, \tag{2.11}$$

in which matrix $\boldsymbol{D}$ represents material constitutive relationship and ρ is density. The assembly process is the same as in standard FEM, except that weak and strong enrichments are incorporated

$$\boldsymbol{M} = \mathop{\mathbb{A}}_e \boldsymbol{m}_e, \qquad \boldsymbol{K} = \mathop{\mathbb{A}}_e \boldsymbol{k}_e, \qquad \boldsymbol{F} = \mathop{\mathbb{A}}_e \boldsymbol{f}_e. \tag{2.12}$$

2.3. Dynamic Integration Schemes

The Discontinuity-enriched Finite Element Method introduced in Section 2.2 spatially discretizes the governing equation. However, time is also evolving in our problem so a method to properly discretize time is also needed. In this study, the time integration schemes used are Newmark type methods and Bathe's method.

2.3.1. Newmark Method

Newmark [30] is a family of methods, where the concrete procedure depends on the choice of parameters β and γ. The two key formulas of Newmark method to update displacement $\boldsymbol{u}$ and velocity $\dot{\boldsymbol{u}}$ are

$$\dot{\boldsymbol{u}}^{t+\Delta t} = \dot{\boldsymbol{u}}^t + \left[(1-\gamma) \ddot{\boldsymbol{u}}^t + \gamma \ddot{\boldsymbol{u}}^{t+\Delta t} \right] \Delta t, \tag{2.13}$$

$$\boldsymbol{u}^{t+\Delta t} = \boldsymbol{u}^t + \dot{\boldsymbol{u}}^t \Delta t + \left[\left(\frac{1}{2} - \beta \right) \ddot{\boldsymbol{u}}^t + \beta \ddot{\boldsymbol{u}}^{t+\Delta t} \right] \Delta t^2. \tag{2.14}$$

With Equation (2.8), (2.13) and Equation (2.14), we can compute the discrete fields at time $t+\Delta t$. Parameters β and γ determine the stability and accuracy of this method. Newmark methods are unconditionally stable if the following condition is satisfied,

$$\gamma \geq \frac{1}{2}, \qquad \beta \geq \frac{1}{4} \left(\gamma + \frac{1}{2} \right)^2. \tag{2.15}$$

Commonly used implicit Newmark procedure is the constant average acceleration method (trapezoidal rule) with $\beta = 1/4$ and $\gamma = 1/2$. From condition (2.15), trapezoidal rule is unconditionally stable. This property provides convenience because convergence of this time integration scheme is independent of the time step we choose. Hughes suggested to use trapezoidal rule with consistent mass matrix in order to mitigate period errors [31]. Furthermore, some values of γ can provide numerical dissipation. $\gamma = \frac{1}{2}$ leads to no numerical dissipation, whereas values of $\gamma > \frac{1}{2}$ create numerical dissipation [31].

In practice, Newmark method is implemented in the form of *predictor-multi corrector* scheme. In this form, at each time step t, a predictor of the next step $(t+\Delta t)$ is defined as

$$\tilde{\boldsymbol{u}}^{t+\Delta t} = \boldsymbol{u}^t + \Delta t \dot{\boldsymbol{u}}^t + \frac{\Delta t^2}{2} (1-2\beta) \ddot{\boldsymbol{u}}^t, \tag{2.16}$$

$$\tilde{\dot{\boldsymbol{u}}}^{t+\Delta t} = \dot{\boldsymbol{u}}^t + \Delta t (1-\gamma) \ddot{\boldsymbol{u}}^t. \tag{2.17}$$

The predictor provides a guess of the fields at the next time step, which serves as an initial value to the multi-corrector phase, where a loop is achieved to converge to the fields at $t = t+\Delta t$. Let i be the counter of this iteration step, the multi-corrector phase of displacement form (d-form) is listed as followed [32],

- Initialization of predictor

$$\begin{aligned} \boldsymbol{u}_{(0)}^{t+\Delta t} &= \tilde{\boldsymbol{u}}^{t+\Delta t}, \\ \dot{\boldsymbol{u}}_{(0)}^{t+\Delta t} &= \dot{\tilde{\boldsymbol{u}}}^{t+\Delta t}, \\ \ddot{\boldsymbol{u}}_{(0)}^{t+\Delta t} &= \boldsymbol{0}. \end{aligned} \tag{2.18}$$

- At iteration i, assemble residual force vector $\Delta \boldsymbol{F}$ and effective stiffness matrix $\boldsymbol{K}^*$, and form the equation to solve. Note that in our problem there is no damping matrix.

$$\begin{aligned} \Delta \boldsymbol{F} &= \boldsymbol{F}^{t+\Delta t} - \boldsymbol{M}\ddot{\boldsymbol{u}}_{(i)}^{t+\Delta t} - \boldsymbol{K}\boldsymbol{u}_{(i)}^{t+\Delta t}, \\ \boldsymbol{K}^* &= \frac{1}{\beta \Delta t^2}\boldsymbol{M} + \boldsymbol{K}, \\ \boldsymbol{K}^* \Delta \boldsymbol{u} &= \Delta \boldsymbol{F}. \end{aligned} \tag{2.19}$$

- An iterative process to find field values of the next iteration step $i+1$.

$$\begin{aligned} \boldsymbol{u}_{(i+1)}^{t+\Delta t} &= \boldsymbol{u}_{(i)}^{t+\Delta t} + \Delta \boldsymbol{u}, \\ \ddot{\boldsymbol{u}}_{(i+1)}^{t+\Delta t} &= \left(\boldsymbol{u}_{(i+1)}^{t+\Delta t} - \tilde{\boldsymbol{u}}^{t+\Delta t}\right) / \left(\Delta t^2 \beta\right), \\ \dot{\boldsymbol{u}}_{(i+1)}^{t+\Delta t} &= \dot{\tilde{\boldsymbol{u}}}^{t+\Delta t} + \Delta t \gamma \ddot{\boldsymbol{u}}_{(i+1)}^{t+\Delta t}. \end{aligned} \tag{2.20}$$

- If the process does not converge, we return to Equation (2.19). Otherwise the convergence loop is ended and the displacement, velocity and acceleration fields at time step $t = t+\Delta t$ are $\boldsymbol{u}_{(i+1)}^{t+\Delta t}$, $\dot{\boldsymbol{u}}_{(i+1)}^{t+\Delta t}$, and $\ddot{\boldsymbol{u}}_{(i+1)}^{t+\Delta t}$, respectively.

2.3.2. Bathe's Method

Sometimes Newmark method may fail to provide accurate results for velocity and acceleration [33]. In these cases, alternative could be to use the Bathe's method. It is a composite time integration scheme that subdivides a complete time step t into two substeps. For the first substep, the trapezoidal rule is used and for the second substep, three-point Euler backward method is applied, which results in the following approximation equations [33]

$$\begin{aligned} \dot{\boldsymbol{u}}^{t+\Delta t/2} &= \dot{\boldsymbol{u}}^{t} + \frac{\Delta t}{4}\left(\ddot{\boldsymbol{u}}^{t} + \ddot{\boldsymbol{u}}^{t+\Delta t/2}\right), \\ \boldsymbol{u}^{t+\Delta t/2} &= \boldsymbol{u}^{t} + \frac{\Delta t}{4}\left(\dot{\boldsymbol{u}}^{t} + \dot{\boldsymbol{u}}^{t+\Delta t/2}\right), \\ \dot{\boldsymbol{u}}^{t+\Delta t} &= \frac{1}{\Delta t}\boldsymbol{u}^{t} - \frac{4}{\Delta t}\boldsymbol{u}^{t+\Delta t/2} + \frac{3}{\Delta t}\boldsymbol{u}^{t+\Delta t}, \\ \ddot{\boldsymbol{u}}^{t+\Delta t} &= \frac{1}{\Delta t}\dot{\boldsymbol{u}}^{t} - \frac{4}{\Delta t}\dot{\boldsymbol{u}}^{t+\Delta t/2} + \frac{3}{\Delta t}\dot{\boldsymbol{u}}^{t+\Delta t}. \end{aligned} \tag{2.21}$$

Using Equation (2.21) and considering we are only dealing with linear problems, the governing equation of dynamics becomes

$$\begin{aligned} \boldsymbol{K}_1 \boldsymbol{u}^{t+\Delta t/2} &= \boldsymbol{F}_1, \\ \boldsymbol{K}_2 \boldsymbol{u}^{t+\Delta t} &= \boldsymbol{F}_2, \end{aligned} \tag{2.22}$$

from which displacements at time $t+\Delta t$ and $t+\frac{1}{2}\Delta t$ can be obtained. Then substitute them to Equation (2.21) and we can obtain displacement, velocity and acceleration fields at time $t+\Delta t$. The details for matrices $\boldsymbol{K}_1$ and $\boldsymbol{K}_2$ and vectors $\boldsymbol{F}_1$ and $\boldsymbol{F}_2$ are expressed as followed [33],

$$\begin{aligned} \boldsymbol{K}_1 &= \frac{16}{\Delta t^2}\boldsymbol{M} + \boldsymbol{K}, \\ \boldsymbol{K}_2 &= \frac{9}{\Delta t^2}\boldsymbol{M} + \boldsymbol{K}, \end{aligned} \tag{2.23}$$

$$\begin{aligned} \boldsymbol{F}_1 &= \boldsymbol{F}^{t+1/2\Delta t} + \boldsymbol{M}\left(\frac{16}{\Delta t^2}\boldsymbol{u}^{t} + \frac{8}{\Delta t}\dot{\boldsymbol{u}}^{t} + \ddot{\boldsymbol{u}}^{t}\right), \\ \boldsymbol{F}_2 &= \boldsymbol{F}^{t+\Delta t} + \boldsymbol{M}\left(\frac{12}{\Delta t^2}\dot{\boldsymbol{u}}^{t+\Delta t/2} - \frac{3}{\Delta t^2}\boldsymbol{u}^{t} + \frac{4}{\Delta t}\dot{\boldsymbol{u}}^{t+\Delta t/2} - \frac{1}{\Delta t}\dot{\boldsymbol{u}}^{t}\right). \end{aligned} \tag{2.24}$$

Stability and accuracy of Bathe's method are addressed in [33, 34]. Implementing this method for linear problems is straightforward and it is a suitable candidate for time integration of linear problems.

2.4. Evaluation of Dynamic Stress Intensity Factors

Stress intensity factors are key parameters in fracture that define the strength of crack tip fields and also gives a criterion for crack propagation. In linear elastodynamic fracture mechanics, the stress intensity factors of modes I and II in polar coordinates r and θ originated at the crack tip are defined as [8]

$$K_1^{\text{dyn}} = \lim_{r\to 0} \sqrt{2\pi r}\sigma_{yy} \qquad \text{at } \theta = 0, \tag{2.25}$$

$$K_2^{\text{dyn}} = \lim_{r\to 0} \sqrt{2\pi r}\sigma_{xy} \qquad \text{at } \theta = 0, \tag{2.26}$$

where σ_{yy} and σ_{xy} are stress components defined in the Cartesien coordinates at crack tip with x axis along the crack and y axis perpendicular to the crack. K_1^{dyn} and K_2^{dyn} are dynamic SIFs for modes I and II, respectively. From these equations, it can be seen that the values of the dynamic stress intensity factors are difficult to evaluate. Therefore, similar to what has been done in quasi-static case, K_1^{dyn} and K_2^{dyn} are evaluated through a dynamic interaction integral, which was proposed by Attigui [18] and Réthoré [19]. The dynamic interaction integral I^{int} is domain-independent and takes the form

$$\begin{aligned} I^{int} = &-\int_A \left\{ \left(\boldsymbol{\sigma}^{\text{aux}} : \nabla \boldsymbol{u} - \rho \dot{\boldsymbol{u}} \dot{\boldsymbol{u}}^{\text{aux}}\right)\left(\boldsymbol{\nabla}\cdot\boldsymbol{q}\right) - \left[\boldsymbol{\sigma}^{\text{aux}} : \left(\nabla \boldsymbol{u} \nabla \boldsymbol{q}\right) + \boldsymbol{\sigma} : \left(\nabla \boldsymbol{u}^{\text{aux}} \nabla \boldsymbol{q}\right)\right] \right\} \mathrm{d}S \\ &+ \int_A \left[\left(\boldsymbol{\nabla}\cdot\boldsymbol{\sigma}^{\text{aux}}\right) \nabla \boldsymbol{u}\left(\boldsymbol{q}\right) + \rho \ddot{\boldsymbol{u}} \nabla \boldsymbol{u}^{\text{aux}}\left(\boldsymbol{q}\right) + \rho \dot{\boldsymbol{u}}^{\text{aux}} \nabla \dot{\boldsymbol{u}}\left(\boldsymbol{q}\right) + \rho \dot{\boldsymbol{u}} \nabla \dot{\boldsymbol{u}}^{\text{aux}}\left(\boldsymbol{q}\right) \right] \mathrm{d}S \end{aligned} \tag{2.27}$$

where A is the integration domain chosen to evaluate the dynamic interaction integral and its boundary ∂A should enclose the crack tip. The superscript *aux* denotes the auxiliary field, which can be chosen to be any dynamic crack tip field. In this study, single mode dynamic tip fields from Nishioka [35] and Freund [8] are used. $\boldsymbol{q}$ is a vector field called *virtual crack extension field*. $\boldsymbol{q}$ is supposed to be tangent to crack surface everywhere in the integration domain. The properties this vector field should satisfy are

- Magnitude of $\boldsymbol{q}$ equals one at the crack tip,
- Magnitude of $\boldsymbol{q}$ equals zero on the boundary of integration domain ∂A,
- $\boldsymbol{q}$ is tangent to the crack surfaces everywhere.

It can be noticed that the shape of crack segments in integration domain A could be complicated, which makes an analytical expression of virtual crack extension field $\boldsymbol{q}$ difficult to find. Therefore, in this study, we are going to construct this field numerically. The process of constructing $\boldsymbol{q}$ is as follows:

1. Compute magnitude of $\boldsymbol{q}$: the magnitude is constructed the same way as constructing weight function of quasi-static interaction integral [26]. Draw a circle centered at the crack tip with radius r denoting the radius of the integration domain. Magnitude of $\boldsymbol{q}$ is exactly 1 in elements completely enclosed by the circle. Elements cut by the circle are called intersected elements. Magnitude of $\boldsymbol{q}$ linearly decreases to 0 at nodes that are outside the circle in the intersected elements.

2. Compute direction of $\boldsymbol{q}$: for any point in the integration domain, find the closest point on the crack. The direction is the same as the tangent to this point on the crack.

3. Evaluate divergence and gradient of $\boldsymbol{q}$: for any point P, two points P_1 and P_2 that are extremely close to it along x and y directions are found. Spatial derivatives of $\boldsymbol{q}$ at P are computed in combination with P_1 and P_2 by finite differences.

Virtual crack extension field constructed by the above method is shown in Figures 2.2 and 2.3. The red line is the crack and the blue arrows show both direction and magnitude of $\boldsymbol{q}$. It can be seen that the virtual crack extension fields constructed by the aforementioned method satisfy the conditions.

The interaction integral can also be related to dynamic stress intensity factors. Starting from the expression of energy release rate [8] and following the same procedure as in the quasi-static case [13], we achieve the expression of dynamic interaction integral in terms of dynamic stress intensity factors [19, 20]:

$$I^{\text{int}} = \frac{2\left(1-\nu^2\right)}{E}\left(f_1(\dot{a})K_1^{\text{dyn}}K_1^{\text{aux}} + f_2(\dot{a})K_2^{\text{dyn}}K_2^{\text{aux}}\right), \tag{2.28}$$

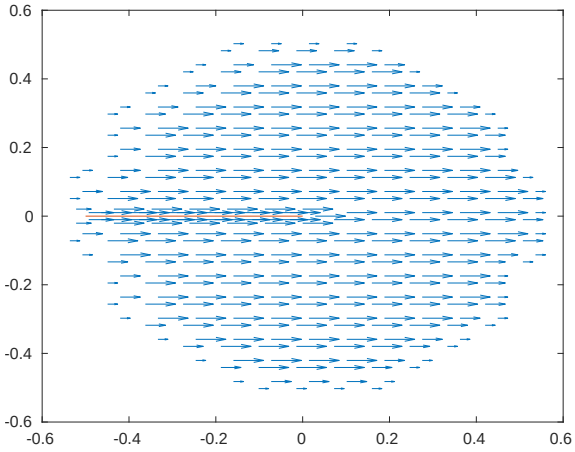

Figure 2.2: Virtual crack extension field near a straight crack.

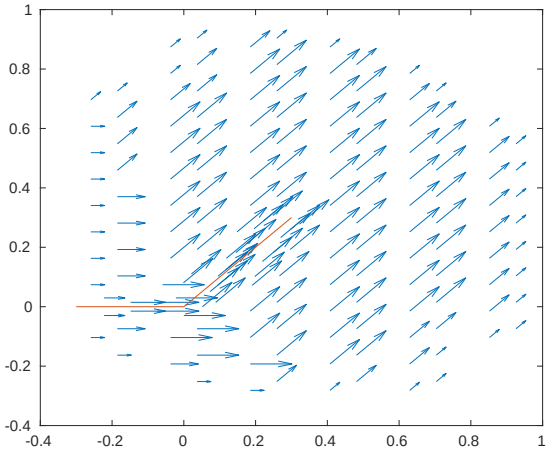

Figure 2.3: Virtual crack extension field near a curved crack.

in which E is Young's modulus, ν is Poisson's ratio, and $\dot{a}$ is propagation speed. Here, $f_1(\dot{a})$ and $f_2(\dot{a})$ are two universal functions that are solely dependent on $\dot{a}$ and independent of crack topology. The expressions of the universal functions are

$$f_1(\dot{a}) = \frac{4\alpha_1\left(1-\alpha_2^2\right)}{(\kappa+1)\,D(\dot{a})}, \qquad f_2(\dot{a}) = \frac{4\alpha_2\left(1-\alpha_2^2\right)}{(\kappa+1)\,D(\dot{a})}, \tag{2.29}$$

where κ is Kolosov's coefficient and α_1 and α_2 are speed parameters given by

$$\alpha_1 = \sqrt{1-\frac{\dot{a}^2}{c_1^2}}, \qquad \alpha_2 = \sqrt{1-\frac{\dot{a}^2}{c_2^2}}. \tag{2.30}$$

c_1 and c_2 are the dilatational and shear wave speeds, respectively. Parameter $D(\dot{a})$ in Equation (2.29) is given by

$$D(\dot{a}) = 4\alpha_1\alpha_2 - \left(1+\alpha_2^2\right)^2. \tag{2.31}$$

Equation $D(\dot{a}) = 0$ is called Rayleigh equation and it has two roots, one is $\dot{a} = 0$ and the other is Rayleigh wave speed $\dot{a} = c_r$, which is the maximum speed a crack can attain during propagation in a homogeneous body.

Equation (2.28) in combination with Equation (2.27) can be used to evaluate dynamic stress intensity factors numerically by properly choosing the auxiliary field. If we are evaluating K_1^{dyn}, the auxiliary field is chosen to be pure mode I dynamic crack tip field with $K_1^{\text{aux}} = 1$ and $K_2^{\text{aux}} = 0$. Similarly, for evaluating K_2^{dyn}, $K_1^{\text{aux}} = 0$ and $K_2^{\text{aux}} = 1$ are chosen. Details of dynamic crack tip fields are elaborated in Appendix B. It is worth to mention that in order to calculate the dynamic interaction integral in Equation (2.27), a large number of Gauss points is required because the dynamic crack tip fields contain trigonometric functions.

2.5. Crack Propagation Method

In order to propagate cracks with DE-FEM, there are three questions to be answered in this section. Firstly, what is the condition for a crack to propagate? Secondly, what is the propagation length and angle for each propagation step? Thirdly, how to map the DOFs at current propagation step to the next when new DOFs are appended due to crack advance?

2.5.1. Determination of Propagation Angle and Speed

The crack propagation criterion was proposed by Griffith [36] and Irwin [37], which says that crack propagates when the stress intensity factor K is large enough that it attains fracture toughness K_c. K_c is a material property and is independent of the problem we are dealing with. In this study, we use the maximum hoop stress criterion to determine propagation direction, which states the crack propagates along the direction of maximum hoop stress $\sigma_{\theta\theta}$ if the equivalent stress intensity factor along this direction $K_{\theta\theta}^{\text{equ}}$ attains K_c. The

direction of maximum hoop stress is evaluated by dynamic stress intensity factors [20, 22]

$$\theta_h = 2\arctan\left(\frac{1}{4}\left(\frac{K_1^{\text{dyn}}}{K_2^{\text{dyn}}} - sign\left(K_2^{\text{dyn}}\right)\sqrt{8+\left(\frac{K_1^{\text{dyn}}}{K_2^{\text{dyn}}}\right)^2}\right)\right). \tag{2.32}$$

Then the equivalent stress intensity factor at this direction, which physically describes the equivalent loading strength at the tip for a mixed mode crack, can be expressed as [20, 22]

$$K_{\theta\theta}^{\text{equ}} = \cos^3\left(\frac{\theta_h}{2}\right)K_1^{\text{dyn}} - \frac{3}{2}\cos\left(\frac{\theta_h}{2}\right)\sin(\theta_h)K_2^{\text{dyn}}. \tag{2.33}$$

The crack speed is determined by

$$\dot{a} = \begin{cases} 0 & \text{when } K_{\theta\theta}^{\text{equ}} < K_c, \\ \left(1 - \frac{K_c}{K_{\theta\theta}^{\text{equ}}}\right)c_r & \text{when } K_{\theta\theta}^{\text{equ}} \geq K_c. \end{cases} \tag{2.34}$$

Equation (2.32), (2.33) and (2.34) are key for determining dynamic crack propagation and they are widely used [20–23, 38, 39]. Once the propagation speed is determined, the propagation length l at this time step can be computed by $l = \dot{a} \times \Delta t$.

2.5.2. An Energy-conserving Scheme for Dynamic Crack Propagation with DE-FEM

In the previous subsection, the length and angle of propagation is set. Following the procedure discussed above, the finite element mesh of DE-FEM changes during propagation because the structure changes as the crack advances. The description of the crack by DE-FEM is updated in this process. Therefore, the enrichment functions that span the finite element space of DE-FEM also vary through propagation. The third question mentioned at the beginning of this section is how to find an appropriate mapping of DOFs for each step of crack propagation in order to make fields properly transfered between time steps.

The idea follows Réthoré's work in which an energy conserving scheme for updating degrees's of freedom in X/GFEM was proposed [19]. In the framework of DE-FEM, updating procedure from step t to step $t+\Delta t$ is summarized as follows:

1. Store displacement, velocity and acceleration fields at current time step $\boldsymbol{u}^t$, $\dot{\boldsymbol{u}}^t$ and $\ddot{\boldsymbol{u}}^t$,

2. At the end of step t, propagate the crack and find new enriched nodes on the background mesh edges. In the mean time, add enrichment functions, which are corresponding to the newly added nodes, to the finite element function space,

3. Initialize displacement, velocity and acceleration associated with new nodes to $\mathbf{0}$ and append them to $\boldsymbol{u}^t$, $\dot{\boldsymbol{u}}^t$ and $\ddot{\boldsymbol{u}}^t$. The appended fields are denoted by $\boldsymbol{u}_n^t$, $\dot{\boldsymbol{u}}_n^t$ and $\ddot{\boldsymbol{u}}_n^t$,

$$\begin{aligned} \boldsymbol{u}_n^t &= [\boldsymbol{u}^t, \mathbf{0}]^\top, \\ \dot{\boldsymbol{u}}_n^t &= [\dot{\boldsymbol{u}}^t, \mathbf{0}]^\top, \\ \ddot{\boldsymbol{u}}_n^t &= [\ddot{\boldsymbol{u}}^t, \mathbf{0}]^\top, \end{aligned} \tag{2.35}$$

4. At step $t+\Delta t$, solve the problem using the updated FE space. Fields $\boldsymbol{u}_n^t$, $\dot{\boldsymbol{u}}_n^t$ and $\ddot{\boldsymbol{u}}_n^t$ are used as input values of displacement, velocity, and acceleration, respectively, from previous time step n. Then continue with step 1 for the next time step.

The above procedure is illustrated in Figure 2.4. At the instance of crack propagation, a new strong node is added on top of the original crack tip, where a weak node already exists. The original crack tip is transformed to a DE-FEM crack segment node. The other nodes along the newly added crack segment are created the same way as indicated in Section 2.2, namely a weak node is created at the new crack tip, and both a strong and a weak node at the intersections between new crack segment and the background element edges.

This procedure can be proven to be energy-conserving because it properly transfers kinetic and potential energy between end of step t and start of step $t+\Delta t$, in which different finite element base functions are used. The kinetic energy at the end of step t with the new crack segment, denoted by T_n^t, is

$$\begin{aligned} T_n^t &= \frac{1}{2}\dot{\boldsymbol{u}}_n^{t\top}\boldsymbol{M}^{t+\Delta t}\dot{\boldsymbol{u}}_n^t = \frac{1}{2}\begin{bmatrix}\dot{\boldsymbol{u}}^t & \boldsymbol{0}\end{bmatrix}\begin{bmatrix}\boldsymbol{M}_{pp} & \boldsymbol{M}_{pq}\\ \boldsymbol{M}_{qp} & \boldsymbol{M}_{qq}\end{bmatrix}\begin{bmatrix}\dot{\boldsymbol{u}}^t\\ \boldsymbol{0}\end{bmatrix} \\ &= \frac{1}{2}\dot{\boldsymbol{u}}^{t\top}\boldsymbol{M}_{pp}\dot{\boldsymbol{u}}^t = \frac{1}{2}\dot{\boldsymbol{u}}^{t\top}\boldsymbol{M}^t\dot{\boldsymbol{u}}^t = T^t \end{aligned} \tag{2.36}$$

Similarly, the potential energy W_n^t at the end of step t with new crack segment is

$$\begin{aligned} W_n^t &= \frac{1}{2}\boldsymbol{u}_n^{t\top}\boldsymbol{K}^{t+\Delta t}\boldsymbol{u}_n^t = \frac{1}{2}\begin{bmatrix}\boldsymbol{u}^t & \boldsymbol{0}\end{bmatrix}\begin{bmatrix}\boldsymbol{K}_{pp} & \boldsymbol{K}_{pq}\\ \boldsymbol{K}_{qp} & \boldsymbol{K}_{qq}\end{bmatrix}\begin{bmatrix}\boldsymbol{u}^t\\ \boldsymbol{0}\end{bmatrix} \\ &= \frac{1}{2}\boldsymbol{u}^{t\top}\boldsymbol{K}_{pp}\boldsymbol{u}^t = \frac{1}{2}\boldsymbol{u}^{t\top}\boldsymbol{K}^t\boldsymbol{u}^t = W^t \end{aligned} \tag{2.37}$$

The subscript p denotes entries corresponding to DOFs before propagating and q means entries corresponding to DOFs after propagation. It can be concluded from Equation (2.36) and (2.37) that the kinetic and potential energies do not change while new DOFs are appended to the mesh and new enrichment functions are added to the space during propagation. This property enables DE-FEM to properly propagate a crack.

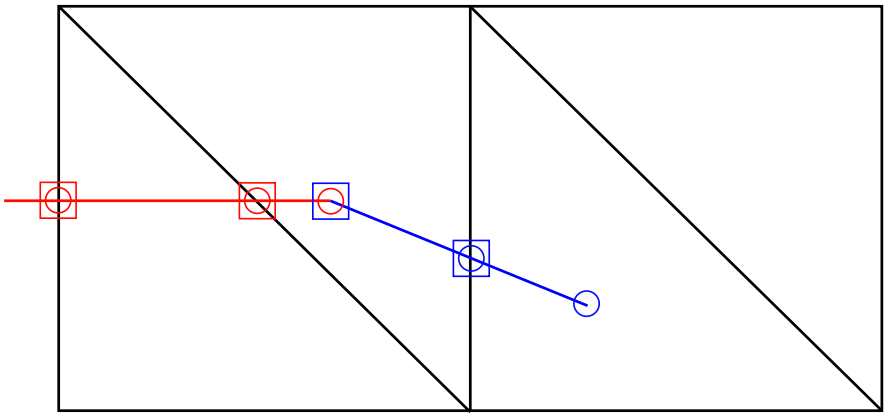

Figure 2.4: Illustration of DOFs mapping procedure by DE-FEM. Four triangle elements are taken as background mesh. Red and blue lines are old crack and propagated segment, respectively. Red and blue circles are old and new weak nodes. Red and blue squares are old and new strong nodes.

DE-FEM has advantages over X/GFEM regarding crack propagation. In X/GFEM, crack tip is enriched with four enrichment functions at each enriched node. Under this energy-conserving scheme, while adding new enriched nodes, a lot of new DOFs are added to the system increasing computational cost. In contrast, DE-FEM only adds a limited number of nodes, associated with only one enrichment function for each node, which reduces the computational cost compared to X/GFEM. Moreover, in DE-FEM, transforming the old crack tip node into the crack segment node is smoother because crack tip enrichment is incorporated in crack segment enrichment. However, in X/GFEM, the crack tip node is transformed to surface node by adding Heaviside enrichment on top of tip enrichment, resulting in a segment node containing tip enrichment that is not supposed to belong to it.

2.6. Numerical Examples

In this section, two kinds of numerical examples are shown. Examples of stationary crack with dynamic loading show evaluations of dynamic stress intensity factors by DE-FEM, and examples of dynamic crack propagation present capability of DE-FEM on simulating dynamic crack growth. In all these examples, three-node triangle elements are used.

2.6.1. Mode I Stationary Crack with Dynamic Loading

In this example, a pure mode I crack subjected to dynamic loading is studied. The problem is a rectangle plane containing a crack, as depicted in Figure 2.5. The rectangle has length $L = 10m$ and width $2H = 4m$. Length of

crack is $a = 5m$. Bottom edge is fixed, and left and right edges are fixed in horizontal direction. An uniformly distributed tensile stress is applied on top edge of the structure with magnitude of $\sigma_0 = 500kPa$. The crack is kept stationary over time. The structure is assigned with material of Young's modulus $E = 210GPa$, Poisson's ratio $\nu = 0.3$ and density $\rho = 8000kg/m^3$. The analytical solution of mode I stress intensity factor is provided by Freund[8] with c_d being dilatational wave speed

$$K_1^{\text{dyn}} = \begin{cases} 0 & \text{if } t \le t_c \\ \frac{2\sigma_0}{1-\nu}\sqrt{\frac{c_d(t-t_c)(1-2\nu)}{\pi}} & \text{if } t_c < t \le t_{max} \end{cases}. \tag{2.38}$$

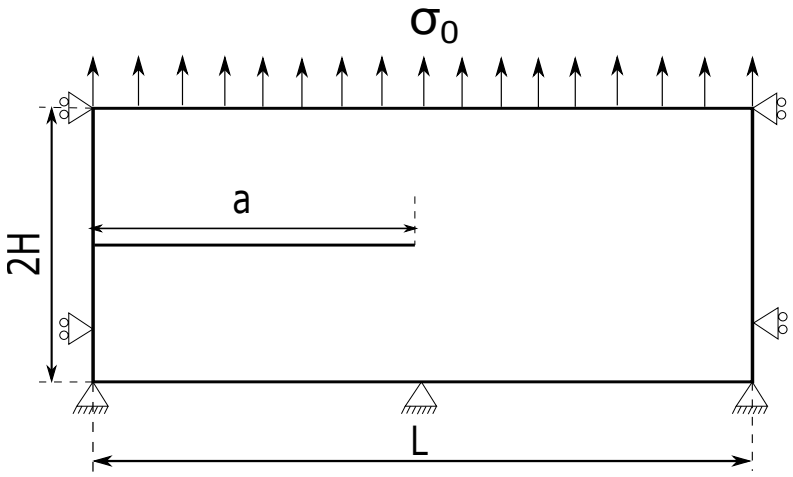

Figure 2.5: Geometry of mode I crack example.

The value of K_1^{dyn} is 0 before $t_c = H/c_d$ because the dilatational wave does not reach the crack until t_c. As Equation (2.38) does not consider reflected stress waves by top and bottom edges, it holds only before the reflected stress waves enter the integration domain of dynamic interaction integral (2.27) at t_{max}. Therefore,

$$t_{max} = \frac{3H - r}{c_d}, \tag{2.39}$$

where r is radius of integration domain and in this example is chosen as $r = 0.6m$. Figure 2.6 shows the results of mode I stress intensity factor K_1^{dyn} in time with a structured mesh of 115×65, where K_1^{dyn} is normalized by $\sigma_o\sqrt{H}$ and time t is normalized by t_c.

It can be observed in Figure 2.6 that K_1^{dyn} has some oscillations near the analytical solution. This can be explained by the intrinsic noise of Newmark constant average acceleration method. This method fails to provide converged results of velocity and acceleration fields in this example. Therefore, Bathe's method is used to mitigate oscillations of these fields, and the oscillations in K_1^{dyn} can be removed as shown in Figure 2.7. Moreover, the stress field obtained by this method is smoother than that by Newmark constant average acceleration method. Figure 2.9 shows the stress distribution obtained by Bathe's method, in which the stress does not show the unrealistic wave patterns as obtained by Newmark in Figure 2.8. Due to the advantage of Bathe's method, it is used for time integration in the following examples.

2.6.2. Mixed Mode Stationary Crack with Dynamic Loading

Stress intensity factors of a mixed mode stationary crack with constant velocity impact is studied. This is a popular example to show evaluation of dynamic stress intensity factors [19, 22, 40]. The model is shown in Figure 2.10. The structure has geometry of $L = 4m$ and $H = 6m$. The crack length is $a = 1m$ located at middle of left edge. A constant velocity $V_0 = 16.5m/s$ is applied at left edge. The material properties are Young's modulus $E = 200GPa$, Poisson's ratio $\nu = 0.25$ and density $\rho = 7833kg/m^3$. The structure is fixed at the top and right edges, and the bottom edge is only allowed to move along horizontal direction. The analytical

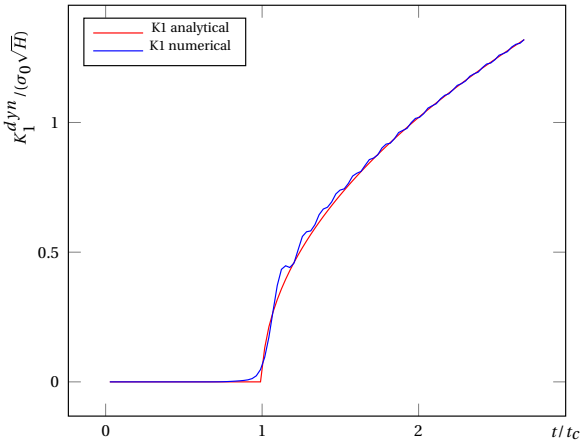

Figure 2.6: Evolution of K_1^{dyn} in time with 115×65 by Newmark constant average acceleration method.

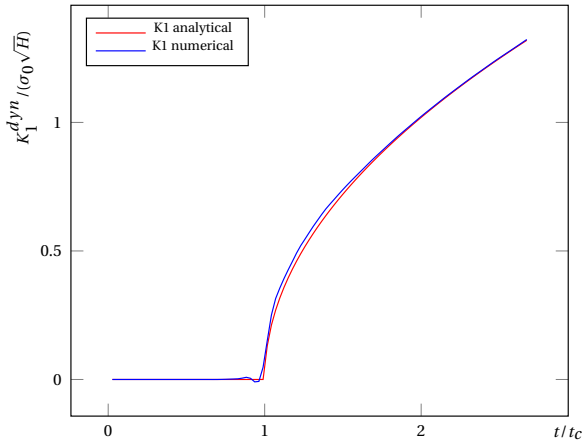

Figure 2.7: Evolution of K_1^{dyn} in time with 115×65 by Bathe's method.

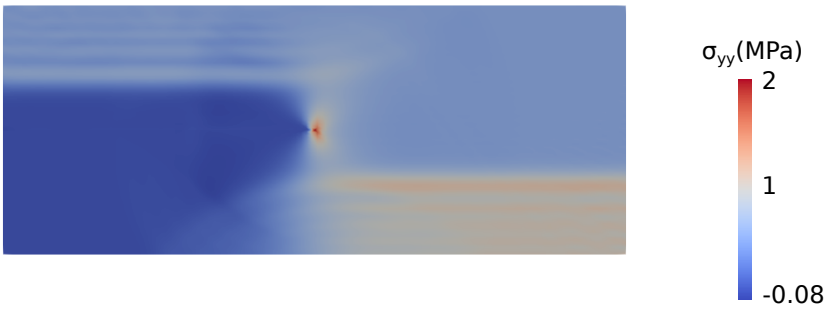

Figure 2.8: σ_{yy} field obtained by Newmark constant average acceleration method at the last time step.

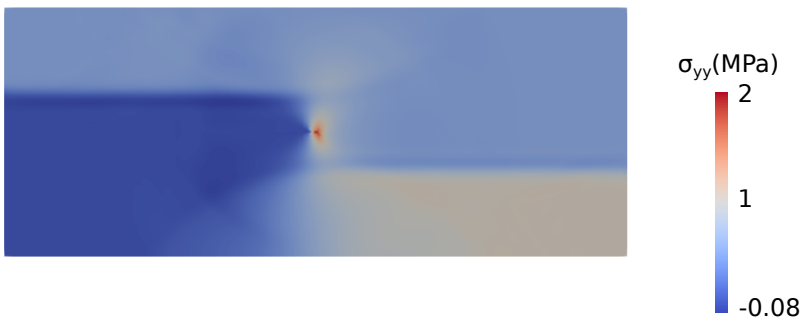

Figure 2.9: σ_{yy} field obtained by Bathe's method at the last time step.

solution is provided by Lee and Freund [41]. Again, the analytical solution does not consider reflected stress waves by edges of structure so it is only valid before $t_{max} = 3a/c_d = 542\mu s$ when reflected wave reaches crack tip.

Figure 2.11 plots the simulation results of this problem with 135×135 structured mesh. The time step of simulation is $\Delta t = t_{max}/60 = 9.033\mu s$. The values of stress intensity factors are normalized by a constant factor $-EV_0\sqrt{a}/(2c_d(1-\nu^2)\sqrt{\pi})$ and the time is normalized by $t_c = a/c_d$. Figure 2.11 shows the numerical result and it is able to reproduce the analytical solution. Therefore, we can conclude that the discontinuity-enriched finite element method is capable of evaluating the stress intensity factors of a mixed mode crack.

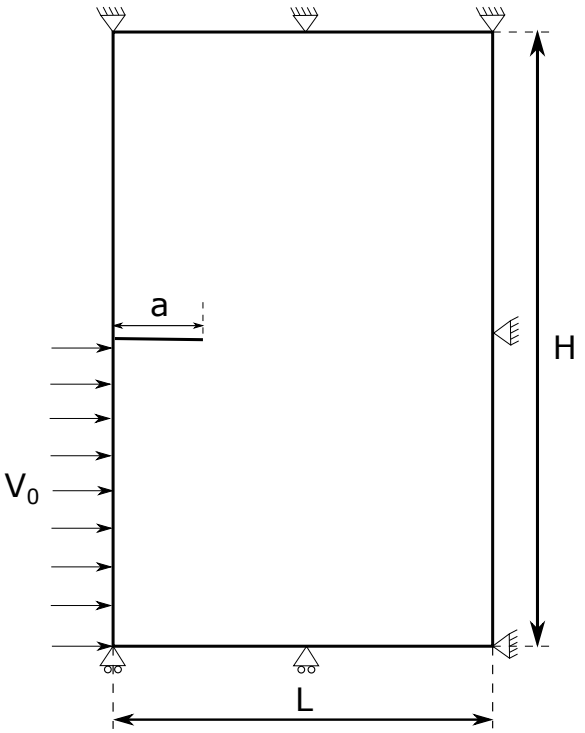

Figure 2.10: Geometry of the mixed mode stationary crack example.

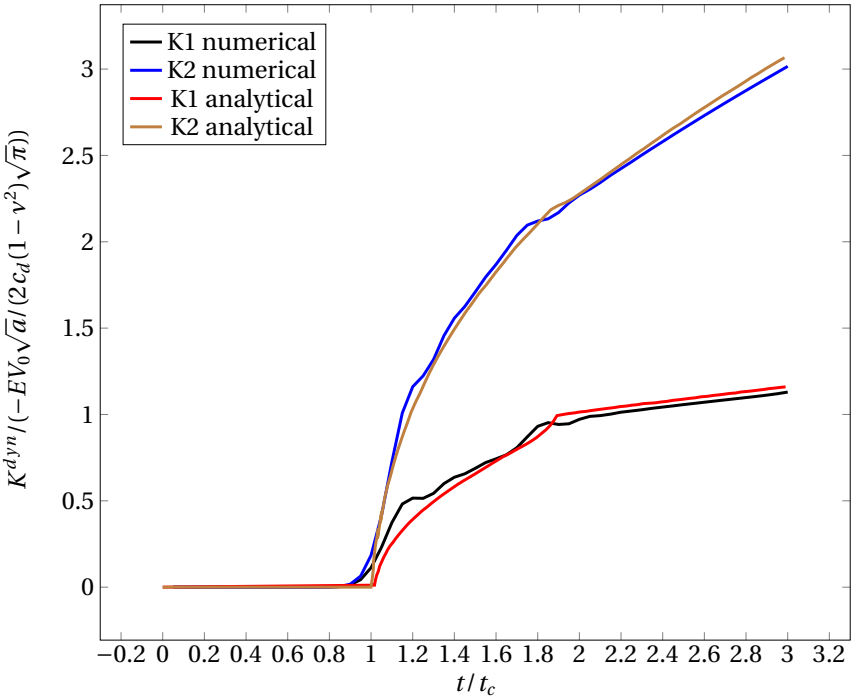

Figure 2.11: Results of evaluation of dynamic stress intensity factors of a mixed mode stationary crack.

2.6.3. First Glance at Dynamic Crack Propagation

Now we move to dynamic crack propagation problems. In this example, the same structure is used as in Section 2.6.1 illustrated in Figure 2.5. However, in this example, we allow the crack to propagate after time $t = 1.5t_c$ with the prescribed horizontal direction and the prescribed speed $\dot{a} = 1500m/s$. This example is

widely studied in order to have first understanding of dynamic crack propagation[19, 21–23]. According to Freund [8], relationship of stress intensity factors of a stationary crack and a propagating crack is

$$K_1^{\text{dyn}}(\dot{a},t) = k(\dot{a})K_1^{\text{dyn}}(0,t), \tag{2.40}$$

where $k(\dot{a})$ is a universal function that is only dependent on the propagation speed. Here, it is approximated by [19, 22]

$$k(\dot{a}) = \frac{1-\frac{\dot{a}}{c_r}}{1-\frac{\dot{a}}{2c_r}}. \tag{2.41}$$

From Equation (2.38) and (2.41), we have the analytical solution for this propagation problem

$$K_1^{\text{dyn}} = \begin{cases} 0 & \text{if } t \le t_c \\ \frac{2\sigma_0}{1-\nu}\sqrt{\frac{c_d(t-t_c)(1-2\nu)}{\pi}} & \text{if } t_c < t \le 1.5t_c \\ \frac{2\sigma_0}{1-\nu}\frac{1-\frac{\dot{a}}{c_r}}{1-\frac{\dot{a}}{2c_r}}\sqrt{\frac{c_d(t-t_c)(1-2\nu)}{\pi}} & \text{if } 1.5t_c < t \le t_{max} \end{cases}. \tag{2.42}$$

In order to model this example properly, a total time of $900\mu s$ and 100 time steps are used to avoid influence of reflected stress waves as discussed in Section 2.6.1. A structured mesh of 115×65 is used and the result is shown in Figure 2.12.

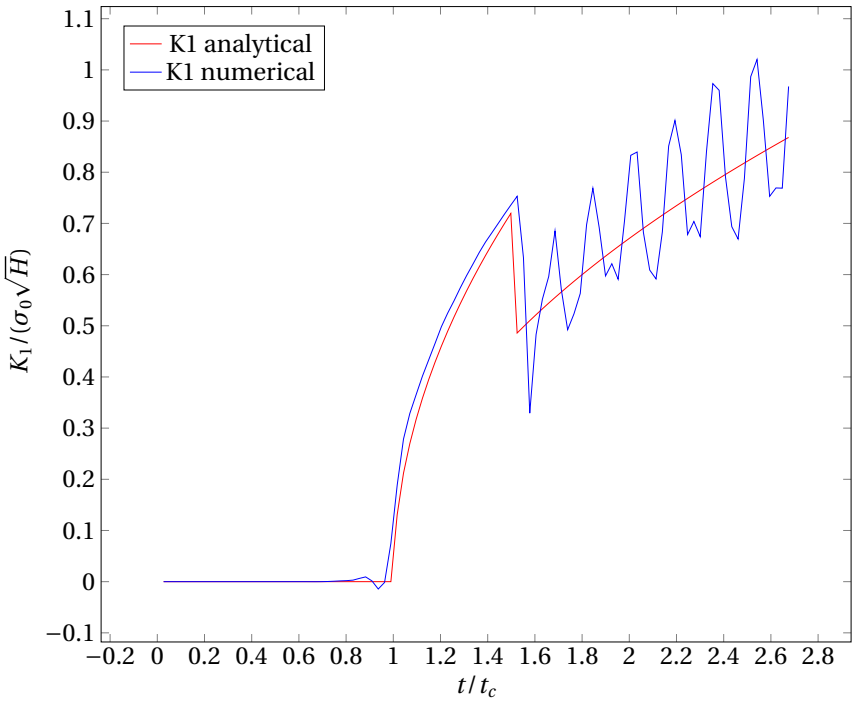

Figure 2.12: Result of stress intensity factor of mode I propagating crack.

It can be seen from Figure 2.12 that after $t = 1.5t_c$, the mode I stress intensity factor shows oscillations. As in this simulation, Bathe's method is used so spurious oscillations of Newmark constant average acceleration method does not exist. Therefore, this kind of oscillations are due to dynamic crack propagation. It is worth to mention that refining mesh cannot reduce level of oscillations. Similar results were also observed by numerical results from Réthoré [19], Wen [22] and Menouillard[21, 23] by X/GFEM. All literature is concluding the oscillations are inevitable. During propagation process, the crack is advanced discontinuously whereas in reality it propagates continuously in time. At each step of crack advance, new crack surface is released suddenly and this discontinuity of the stiffness in time introduces a high-frequency response to the structure near crack tip [19]. The stiffness discontinuity is the reason of oscillations. Menouillard [23] proposed a

smoothed nodal force scheme which enables smoother release of crack surface in order to mitigate discontinuity of stiffness, but due to the intrinsic discontinuity of time integration scheme the oscillations cannot be completely removed. Other attempts like using meshfree method [42] and spectral element method [24] *etc.* cannot tackle this problem properly either. Therefore, we can conclude that dynamic crack propagation will introduce numerical oscillations near crack tip.

2.6.4. Kalthoff Test of Dynamic Crack Propagation

This section discusses dynamic crack propagation of a plate under impact loading. The corresponding experiment was conducted by Kalthoff *et al.* [43] This example has been extensively used in literature to benchmark crack path prediction [14, 17, 19, 20, 44]. In Kalthoff's experiment, two horizontal edge cracks lie on a plate symmetrically. In order to simplify simulation, only half plate including a single crack is considered [20] and the geometry of the structure is shown in Figure 2.13.

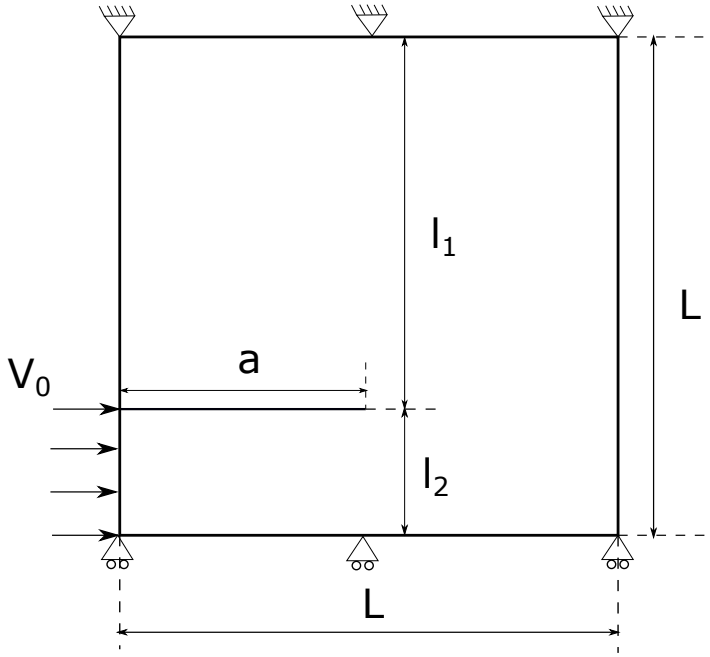

Figure 2.13: Geometry of Kalthoff test used to benchmark crack path prediction.

The geometry parameters of Kalthoff test are given as follows: length $L = 0.1m$ and initial crack lies horizontally at the left edge of the plate with length $a = 0.05m$. l_1 and l_2 are $0.075m$ and $0.05m$, respectively. Impact loading is modeled by a constant velocity applied on the bottom of the left edge as shown in Figure 2.13. Material of the square plate is 18Ni1900 maraging type steel with Young's modulus $E = 190GPa$, Poinsson's ratio $\nu = 0.3$ and density $\rho = 8000kg/m^3$. Fracture toughness is $K_c = 68MPa\sqrt{m}$. At low impact velocity, Kalthoff observed brittle fracture [43]. The crack is supposed to propagate northeasternly with an overall angle of 60 to 70 degrees [20, 22]. However, at high impact velocity, the problem changes intrinsically and brittle fracture is no long there. In this example, we are studying crack propagation in brittle material so impact velocity is chosen to be $V_0 = 20m/s$ [20, 22]. The model is assumed to be plane strain with top edge fixed and bottom edge fixed in vertical direction. The total time of simulation is $t = 100\mu s$ and the time step is $\Delta t = 0.5\mu s$.

Figure 2.14 shows the result of crack path and distribution of the horizontal displacement with mesh of 165×165. The overall angle of crack path with respect to horizon is around 60 degrees, which is in the range of 60 to 70 degrees so it can be concluded that the model can predict crack path. Song also got similar result [17] and the result of angle is better than that obtained by Belytschko [14].

The process of crack propagation and horizontal stress distribution σ_{xx} at instances of $30\mu s$, $50\mu s$, $70\mu s$, and $90\mu s$ are illustrated in Figure 2.15. The singular stress field near crack tip is clearly shown in the simulation, which is in accordance with the linear elastic fracture mechanics [8]. Initially, the crack is propagating

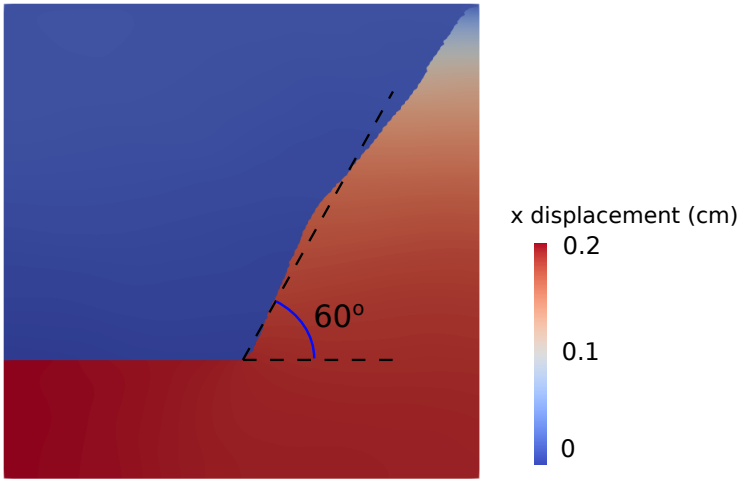

Figure 2.14: Propagation path of Kalthoff test and distribution of x displacement.

with an inclination angle of around 66 degrees, as shown in Figure 2.15b. Then the angle decreases (Figure 2.15c) and this can be explained by the influence of the reflected stress waves from the left edge of the structure. This phenomenon was also observed in the simulation of Réthoré by X/GFEM [19].

If we zoom in to the details of crack surface in Figure 2.16, small zigzags can be observed. Zigzags are produced by oscillations of SIFs discussed in Section 2.6.3. As shown in Figure 2.17, during the time steps that crack propagates, modes I and II SIFs K_1^{dyn} and K_2^{dyn} are both oscillating. K_2^{dyn} oscillates between positive and negative values. Because the direction of crack growth is dependent on the sign of K_2^{dyn} in Equation (2.32), the oscillation induces alternation in the propagation direction and thus causes zigzags on crack surfaces. The positive/negative pairs of K_2^{dyn} correspond with the zig/zag patterns of crack surface. However, from a global view, the level of zigzags is relatively small so generally we still have a smooth crack path. The oscillations make simulation of dynamic crack propagation a challenging topic and it is not as accurate as modeling of quasi-static cracks [22].

2.7. Conclusions

Simulation of dynamic crack propagation has long been a challenging topic in engineering. In this thesis, the novel Discontinuity-enriched Finite Element Method was applied to solve dynamic fractures in brittle materials. Two kinds of problems were analyzed. In the stationary crack with dynamic loading problems, DE-FEM was able to reproduce the analytical SIFs history. In the Kalthoff experiment of dynamic crack propagation example, DE-FEM was capable of predicting the crack path. Therefore, it can be concluded that DE-FEM is a suitable candidate to simulate dynamic fracture problems.

Moreover, the computer implementation of DE-FEM is straightforward when modeling dynamic crack propagation. The crack tip node is associated with a weak node, whereas the crack segment node is endowed with both a strong and a weak node. Therefore, in the computer program, a crack tip node could be transformed to a crack segment node by simply adding a strong node on top of it. This provides simplicity on advancing cracks.

The stress intensity factors were evaluated by a domain-independent dynamic interaction integral. The virtual crack extension field is a key parameter of the dynamic interaction integral. It is a vector field and is constructed numerically by finite difference. Its magnitude is computed exactly the same way as constructing the weight function for quasi-static crack interaction integral [26], providing direct extension of static crack to dynamic crack propagation.

Oscillations of SIFs have been an issue for numerical simulations of dynamic fracture. In this thesis, the oscillations of stationary crack with dynamic loading problems were completely removed. The oscillation issue of this kind of problem was due to the time integration scheme. Newmark constant average acceleration method might fail to provide a converged velocity and acceleration fields [33], and this failure caused

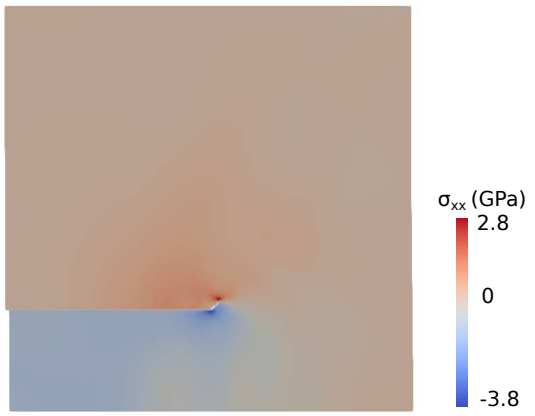

(a) Crack propagation at $t = 30\mu s$.

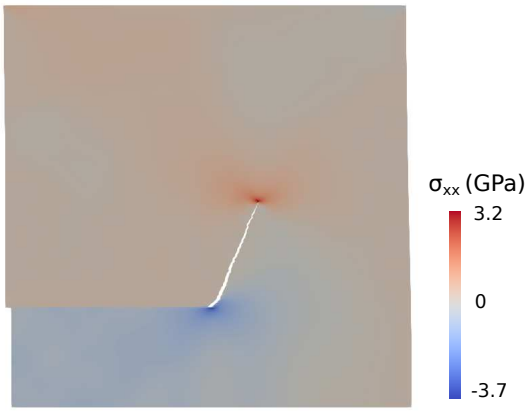

(b) Crack propagation at $t = 50\mu s$.

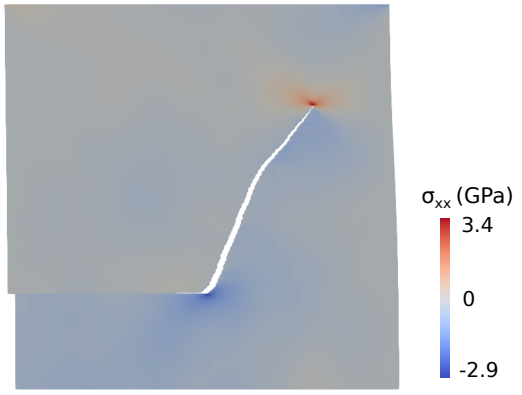

(c) Crack propagation at $t = 70\mu s$.

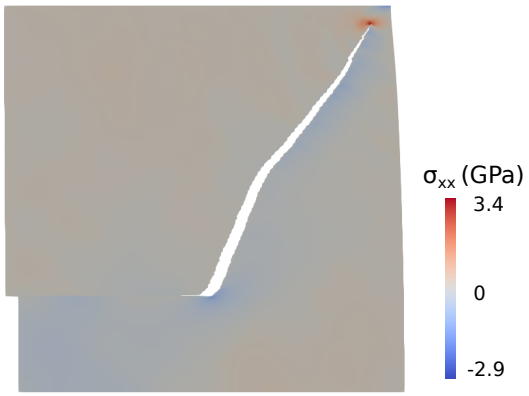

(d) Crack propagation at $t = 90\mu s$.

Figure 2.15: Crack propagation process at four different time instance (magnified by 2 times). The contour here is the horizontal component of stress σ_{xx}.

Figure 2.16: A zoomed in view of crack surface.

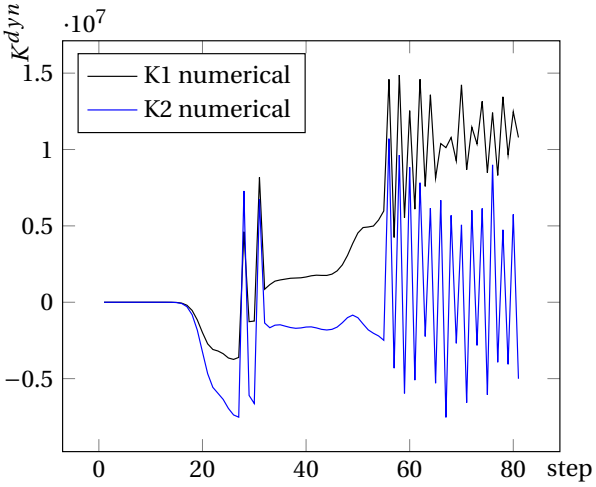

Figure 2.17: Mode I and mode II stress intensity factors until $40\mu s$

oscillations in SIFs. In order to solve it, the Bathe's method was implemented. This is a novel time integration method with better convergence property and can be an alternative when Newmark fails. Therefore, smooth evaluations of SIFs without oscillations were achieved and the stress field did not show the unrealistic wave patterns.

However, for dynamically propagating cracks, the oscillations in SIFs are inevitable. The issue arises not only in DE-FEM, but also in other numerical tools like X/GFEM. This is due to the discontinuity of stiffness in time near crack tip during propagation steps. Better time discretization methods could be preferred in order to release the crack tip more smoothly, and thus get smaller level of oscillations.

3

Reflection

3.1. Chioce of Research Topic

When choosing thesis project in the first year of my master's study, I was intrigued by this interdisciplinary project of crack propagation using discontinuity-enriched finite element method. Fracture problems exist not only in mechanical engineering, but also in civil engineering, aerospace and nuclear *etc.* This property makes the topic versatile and the method developed can be applied to many different fields.

The literature research took me around two months. During this period I read books of foundamentals of fracture mechanics and understood basic definitions and formulas of linear elastic fracture mechanics. I also looked at some stuffs of cracks in plastic materials. Furthermore, I read papers including recent developments in crack propagation. In these papers I found the dynamic crack propagation interesting. Dynamic crack propagation is also a challenging topic as there are still a lot of difficulties like computational cost, spurious oscillations as well as branching and coalescence *etc.*

3.2. Process of Porject

My work started with implementing Newmark method. It was very challenging for me to code with *Hybrida* at the beginning because it was my first time to code in object-oriented software. I spent weeks learning object-oriented programming and basic structures of *Hybrida*. After equipped with required programming knowledges, I started coding dynamic analysis class and Newmark class. The verification of these codes took me too much time because I spent some time learning beam and shell theory. Also the corona virus pandemic forced me to work from home and it had large negative influence on my productivity. After understanding basics of Euler-bernoulli beam and Timoshenko beam theory, I was able to verify my implementation of dynamic class and Newmark class by free and forced vibrations of a cantilever beam. During this process, I also fixed bugs of vectorized assembly of mass matrix of triangle and quadrilateral elements with the help of my PhD senior.

The next task was to compute dynamic interaction integral in order to evaluate SIFs. This task was more challenging than the previous task. The virtual crack extension field took me some time because initially I was trying to find a way to construct it analytically but after some failures did I realize it was much smarter to construct it numerically. With all these ingredients, I was able to compute dynamic stress intensity factors properly.

The third task was to find a way to propagate crack. The class for crack propagation was implemented in *Hybrida* by *visitor design pattern* which could extend functionality of Dynamic codes without changing much of its implementation. Inspired by the energy-conserving scheme, I soon noticed DE-FEM would benefit from it because advancing cracks by this method is straightforward by construction. Therefore, this scheme was adopted to DE-FEM and coded in *Hybrida*. However, the first try of crack propagation was terrible because I re-created crack for each propagation step and the mapping of degrees of freedom from one step to the next was a mess. In order to solve it, I wrote a crack propagation function in *Hybrida* geometric engine to append new crack segment to the old crack. By this function, the old DOFs were preserved and I only needed to append new DOFs at end of displacement, velocity and acceleration vectors. Then the crack path was more reasonable but it still had zigzags on its surface. It tool me long time to understand this phenomenon

for doing literature survey and some numerical tests. It turned out that Newmark constant average acceleration method does not have enough accuracy on velocity and acceleration. Thus Bathe's method was applied to tackle this problem. Although according to literature the zigzags could not be completely removed, this method did help a lot in reducing the level of zigzags in propagation.

During the process of the aforementioned three tasks, my supervisor Alejandro guided me and gave me valuable suggestions. Also my peers and my PhD seniors helped me with coding. I would like to give my sincere gratitude to them.

3.3. Personal Improvement During Thesis Work

The period of working on my thesis project is precious for me because I improved myself during this period, especially my time management skill. Now I understand the importance of finishing tasks as early as possible. In the early phase of my project, I was always thinking time was enough and I still had several months to finish my project. Then it turned out that research was difficult to 'go as planed' because there were always unexpected difficulties and challenges. These difficulties and challenges took me so much unexpected time to deal with. This taught me a good lesson that always reserve enough time when doing anything so that any 'unexpected issue' would not influence the plan.

I also gained a lot of precious skills in scientific research like problem shooting, literature research as well as how to find method to solve my problems *etc.* These skills will benefit me not only for my future research but also for my life.

3.4. Future Work Orientation

My thesis topic has potential to be studied further. In my work, I managed to propagate a single crack dynamically but the interaction of multiple dynamic cracks remains a challenge in elastodynamic fracture mechanics. Also the branching and coalescence behaviors are typical phenomena that happen only when crack propagation is modeled dynamically. Moreover, in addition to Bathe's method, some other tools to further mitigate zigzag issue of crack surface may also be developed in the framework of DE-FEM. Someone may continue my work to further investigate the above problems.

Appendices

A

Fracture Mechanics and Its Numerical Implementations

A.1. Crack Modes

For a three-dimensional crack, under different loading condition, it has three cracking modes [45], as illustrated in Figure A.1.

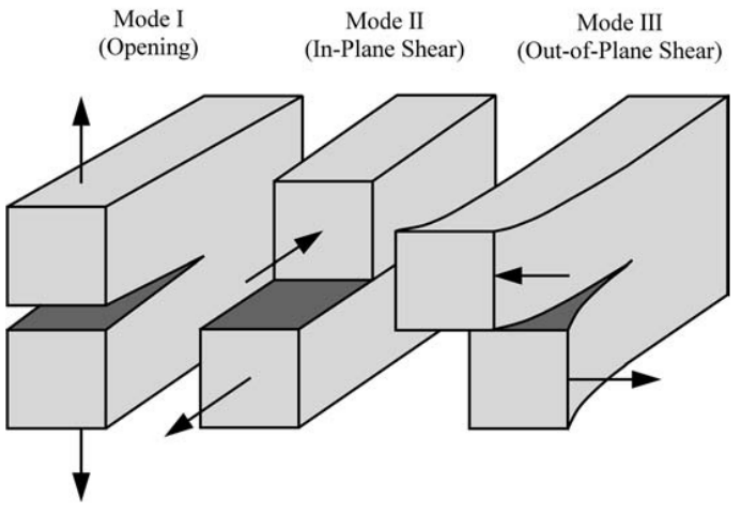

Figure A.1: Three modes of crack. [45]

- Mode I: crack opening mode. This mode corresponds to the scenario that normal pressure is applied to crack surfaces. The upper and lower part of solids are moving perpendicularly to crack surfaces in opposite directions,
- Mode II: in-plane shear mode. In this mode, shear stress is applied parallel to crack surfaces but perpendicular to crack front. Upper and lower part of solids are moving along crack orientation but in opposite directions,
- Mode III: anti-plane shear mode. In this case, shear stress is applied parallel to crack surfaces and crack front. The upper and lower part of solids are moving out-of-plane in opposite directions, tending to tear the structure.

A.2. Quasi-static Crack

When time evolution is not considered for cracked body, for example in case of low loading rate or slow propagation speed, the crack can be considered as quasi-static. Under this condition, governing equation is

static equilibrium and expressed by stress $\boldsymbol{\sigma}$ and external load $\boldsymbol{f}$

$$div(\boldsymbol{\sigma}) + \rho \boldsymbol{f} = 0. \tag{A.1}$$

In linear elastic fracture mechanics, crack tip stress field is solely characterized by stress intensity factor (SIF) K_{sta}

$$\sigma = \frac{K_{sta}}{\sqrt{2\pi r}} f(\theta), \tag{A.2}$$

where r and θ are polar coordinates and $f(\theta)$ represents angular variation of crack tip stress. $f(\theta)$ is an universal function and is dependent only on polar coordinate θ. K_{sta} dictates strength of crack tip field. As can be seen from Equation (A.2), crack tip stress field is singular and it goes to infinite at crack tip. Figure A.2 shows σ_{yy} near mode I crack tip and other components of stress tensor $\boldsymbol{\sigma}$ behaves similarly. This is a key character in linear elastic fracture mechanics. Stress fields of different modes are determined by each stress intensity factor, denoted by K_I, K_{II} and K_{III} respectively and they are uncoupled from each other.

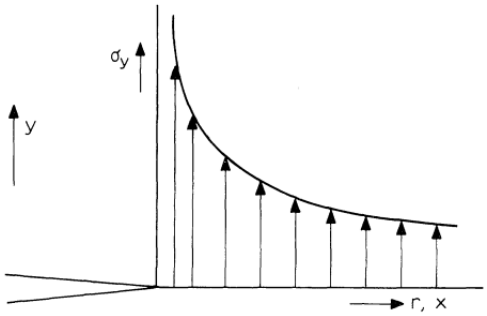

Figure A.2: Integration domain of J integral. [46]

When the crack is propagating, extension of crack surface leads to energy dissipation, which is energy release rate G [36, 37]

$$G = -\frac{d\Pi}{dA}, \tag{A.3}$$

in which A is crack surface area and Π is overall potential energy including internal potential (strain energy) Π_i and external potential (load potential) Π_e

$$\Pi = \Pi_i + \Pi_e. \tag{A.4}$$

Physically, Equation (A.3) means rate of change in potential energy with crack surface area. Since G is derivative of potential, which has dimension of force, G is also called *crack extension force* or *crack driving force* [45]. Energy release rate allows us to consider crack propagation criterion from energy view. During propagation process, potential energy should be large enough to overcome surface energy of material, i.e. energy dissipated to create unit crack surface. Based on this understanding, Griffith [36] gives a criterion for crack propagation: when energy release rate reaches a specific value, denoted by G_c, crack propagates

$$G \geq G_c. \tag{A.5}$$

G_c is called fracture toughness and it is a material property. In linear elastic fracture mechanics, *J-integral* was proposed by Rice [47] to evaluate energy release rate G

$$G = J. \tag{A.6}$$

J-integral is easier to evaluate than Equation (A.3). It is a domain-independent integral evaluated along ∂A, which is boundary of domain A

$$J = \int_{\partial A} (W\delta_{1j} - \sigma_{ij}\frac{\partial u_i}{\partial x_1}) n_j ds, \tag{A.7}$$

with W denotes strain energy expressed as Equation (A.8). σ_{ij} and u_i are stress and displacement respectively. Vector $\boldsymbol{n}$ is directional vector at boundary and towards out of the integration domain.

$$W = \frac{1}{2}\sigma_{ij}\varepsilon_{ij} \tag{A.8}$$

The domain is illustrated in Figure A.3. Its boundary ∂A does not cross crack surface so some part of ∂A is along crack surface, denoted by $\Gamma^{(+)}$ and $\Gamma^{(-)}$

$$\partial A = \Gamma + \Gamma^{(+)} + \Gamma^{(-)}. \tag{A.9}$$

Within regime of linear elastic fracture mechanics, energy release rate can be directly rewritten in terms of stress intensity factors

$$G = \frac{K_I}{E^*} + \frac{K_{II}}{E^*}, \tag{A.10}$$

in which,

$$E^* = \begin{cases} E & \text{for plane stress condition} \\ \dfrac{E}{1-\nu^2} & \text{for plane strain condition} \end{cases}, \tag{A.11}$$

ν is Poisson's ratio. Equation A.10 provides a practically friendly way to evaluate energy release rate. Therefore, propagation criterion A.5 can also be written in terms of stress intensity factors

$$K^* \geq K_c. \tag{A.12}$$

K_c is critical stress intensity factor and K^* is equivalent stress intensity factor. K^* can be evaluated by different ways: the maximum hoop stress criterion [48], the maximum principal stress criterion [49] etc. The criterion stated in Equation (A.12) is widely used: if equivalent stress intensity factor is larger than critical stress intensity factor, the crack propagates.

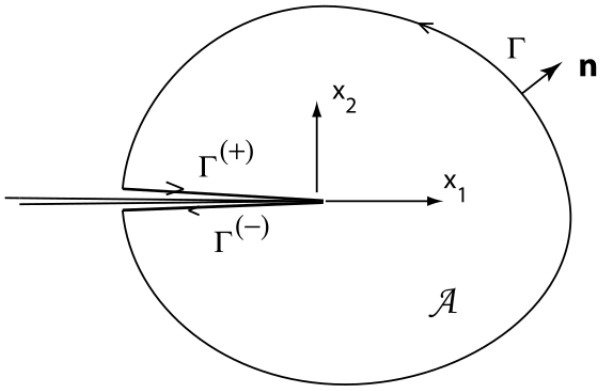

Figure A.3: Integration domain of J integral. [50]

A.3. Dynamic Crack

In practice, all cracks are dynamic and modeling crack as dynamic is better to reflect fracture physics than quasi-static case. Lawn provides two cases in which a crack system may become dynamic [9]

- When a crack reaches a point of instability in its length (crack walls separating rapidly),
- When the applied loading is subject to a rapid time variation, as in impact loading.

Analysis of dynamic crack becomes more complicated compared with quasi-static case. Due to inertia effect, kinetic energy is incorporated in governing equation and energy expression. Also, effect of external load is not applied to each point of structure instantaneously but by means of stress wave. In dynamic case, governing equation of problem is

$$div(\boldsymbol{\sigma}) + \rho \boldsymbol{f} = \rho \ddot{\boldsymbol{u}}. \tag{A.13}$$

Compared with quasi-static case A.1, inertia term $\ddot{\boldsymbol{u}}$ is added to represent kinetic energy.

A.3.1. Stress Waves

Stress waves only show up in dynamic case but not in quasi-static case. If the momentum equation, i.e. governing Equation (A.13), is written in terms of displacement $\boldsymbol{u}$, then we have Navier's equation of motion [8]

$$(\lambda+\mu)\nabla(\nabla\cdot\boldsymbol{u})+\mu\nabla^2\boldsymbol{u}+\rho\boldsymbol{f}=\rho\ddot{\boldsymbol{u}}. \tag{A.14}$$

According to classic field theory, there is following relationship of curl and divergence

$$\nabla\times(\nabla\times\boldsymbol{u})=\nabla(\nabla\cdot\boldsymbol{u})-\nabla^2\boldsymbol{u}, \tag{A.15}$$

Plug Equation (A.15) into Equation (A.14) and we have

$$c_d^2\nabla(\nabla\cdot\boldsymbol{u})-c_s^2\nabla\times(\nabla\times\boldsymbol{u})+\boldsymbol{f}=\ddot{\boldsymbol{u}}, \tag{A.16}$$

where c_d and c_s are written in terms of Lamé constants

$$c_d=\sqrt{\frac{\lambda+2\mu}{\rho}}\quad,\quad c_s=\sqrt{\frac{\mu}{\rho}}. \tag{A.17}$$

Let the body force $\boldsymbol{f}$ equals zero for time being. If divergence operator $\nabla\cdot$ and curl operator $\nabla\times$ are operated on each term of Equation (A.16) respectively, two elementary wave equations are obtained

$$c_d^2\nabla^2(\nabla\cdot\boldsymbol{u})=(\nabla\cdot\boldsymbol{u})_{,tt}\,, \tag{A.18}$$

$$c_s^2\nabla^2(\nabla\times\boldsymbol{u})=(\nabla\times\boldsymbol{u})_{,tt}\,. \tag{A.19}$$

It can be seen from Equation (A.18) and Equation (A.19) that volume change and rotational deformation of points are propagating in structure with speed c_d and c_s respectively. Therefore, c_d is called dilatational wave speed and c_s is called shear wave speed. For dilatational wave, oscillation of particle is along wave propagation direction. If oscillation of a particle is perpendicular to wave direction then it is called shear wave. These two waves are both *body waves*. Stress waves could also be observed in a lot of disciplines but terminology could be different. For example, in seismology, dilational wave and shear wave are also called P wave and S wave respectively.

Another important wave parameter in dynamic crack is Rayleigh wave speed, denoted by c_r. Rayleigh wave is a type of *surface wave* that travels along surface of a solid. Its amplitude decreases exponentially as distance from surface increases [51]. Rayleigh wave speed is related to the maximum propagation speed a crack can attain in solids.

A.3.2. Stress Intensity Factor and Energy Release Rate

For dynamic crack, definition of stress intensity factor is the similar as it in quasi-static case

$$\sigma=\frac{K_{dyn}}{\sqrt{2\pi r}}g(\theta,v), \tag{A.20}$$

except here K_{dyn} represents dynamic stress intensity factor and angular variation function $g(\theta,v)$ is different from its quasi-static counterpart $f(\theta)$. The angular function $g(\theta,v)$ is dependent on crack propagation speed v and it satisfies [8]

$$\lim_{v\to 0}g(\theta,v)=f(\theta), \tag{A.21}$$

which shows physical consistency of quasi-static and dynamic crack. If propagation velocity of a dynamic crack is 0, then it falls into regime of quasi-static crack and they have the same crack tip stress field. In this case, the numerator K_{dyn} in Equation (A.20) becomes static stress intensity factor K_{sta}.

When crack of length a is propagating with speed v, dynamic stress intensity factor is related to static stress intensity factor by

$$K_{dyn}(v,a)=k(v)K(0,a)=k(v)K_{sta}. \tag{A.22}$$

Here, $k(v)$ is an universal function. For a cracked body with given geometry, it is only dependent on propagation speed v. If v is close to 0, then $k(v)\to 1$.

Similar to quasi-static crack, energy release rate is also defined in dynamic crack scenario. The dynamic energy release rate is defined as the rate of mechanical energy flow out of the body and into the crack tip per unit crack advance [8]. Therefore, the dynamic energy release rate is denoted by G_{dyn} and it is defined as

$$G_{dyn} = \lim_{\partial A \to 0} \frac{F(\partial A)\delta t}{v\delta t} = \lim_{\partial A \to 0} \frac{F(\partial A)}{v}, \tag{A.23}$$

where ∂A is curve near crack tip and enclosing crack tip, as depicted by Figure A.3. $v\delta t$ represents unit crack advance and $F(\partial A)\delta t$ is mechanical energy influx. $F(\partial A)$ is the instantaneous rate of energy flow through ∂A toward the crack tip [8], expressed as

$$F(\partial A) = \int_{\partial A} [\sigma_{ji} n_j \frac{\partial u_i}{\partial t} + (U+T) v n_1] ds, \tag{A.24}$$

in which U and T are potential and kinetic energy density respectively.

The dynamic energy release rate in Equation (A.23) can also be related to dynamic stress intensity factors in A.20 [8]

$$G_{dyn} = \frac{1-\nu^2}{E}[A_I(v)K_I^2 + A_{II}(v)K_{II}^2]. \tag{A.25}$$

Equation A.25 holds only for plane strain condition. For plane stress problem, coefficient $\frac{1-\nu^2}{E}$ should be replaced by $\frac{1}{E}$. E and ν are Young's modulus and Poisson's ratio respectively. An important difference of Equation (A.25) from Equation (A.10) is that two universal functions, A_I and A_{II}, are incorporated in order to account for dynamic effect and they are solely functions of propagation speed v

$$A_I(v) = \frac{v^2\alpha_d}{(1-\nu)c_s^2 D} \quad , \quad A_{II}(v) = \frac{v^2\alpha_s}{(1-\nu)c_s^2 D}, \tag{A.26}$$

where α_d and α_s are speed parameters,

$$\alpha_d = \sqrt{1 - \frac{v^2}{c_d^2}} \quad , \quad \alpha_s = \sqrt{1 - \frac{v^2}{c_s^2}}. \tag{A.27}$$

And $D = 4\alpha_d\alpha_s - (1+\alpha_s^2)^2$. $D = 0$ is called Rayleigh equation and solutions to it are $v = 0$ and $v = c_r$, where c_r is the Rayleigh wave speed. A_I and A_{II} are monotonically decreasing when crack speed is increasing. If crack speed $v \to 0$ then these two universal functions are equal to one [8]

$$\lim_{v\to 0} A_I(v) = 1 \quad , \quad \lim_{v\to 0} A_{II}(v) = 1. \tag{A.28}$$

Equation A.28 shows dynamic energy release rate returns to quasi-static case A.10 if crack speed is zero. Theoretical research has shown that crack can never travel faster than Rayleigh wave speed [52]. However, in practice, when crack speed is close to c_r, instability may happen to the system.

A.3.3. Crack Instability

Crack instability is a feature only exists in dynamic crack but not in quasi-static crack. Instability occurs when crack propagation speed is very high. Chen [53] shows that when crack speed attains around 0.92 of shear wave speed ($0.92c_s$), crack tip will start to oscillate. This oscillation is induced by nonlinear elastic regime near crack tip. Fortunately, this thesis is dealing with linear elastic fracture mechanics so this physical crack tip oscillation will not show in this study.

Crack branching is widely observed in nature and this is also an effect of crack instability. When crack is propagating fast, energy influx into crack tip is so large that crack cannot release it by creating just single crack surface. Therefore, crack branches to have more crack surfaces to release the inflowing energy in order to attain energy conservation at crack tip [54]. A sufficient model to calculate branching speed and angle for mixed mode crack of any material is a complicated research topic in fracture mechanics. Based on relationship before and after branching, Adda-Bedia proposed a model to evaluate branching angle and critical speed [55]. However, his model is only applicable for single mode crack and extensions to mixed mode fracture is still not clear. Yoffe noticed that for crack speed less than 60 percent of shear wave speed ($0.6c_s$), the maximum hoop stress has a maximum value along $\theta = 0$, i.e. along propagation direction. However, for crack speeds greater than $0.6c_s$, the maximum hoop stress is measured at about 60° to propagation direction. Yoffe suggested this could be an indication of crack branching [56].

A.4. Numerical Methods for Fracture Problems

There are lots of numerical algorithms to model problems with crack and among them Finite Element Method (FEM) is widely used. Also cohesive element can be used in combination with FEM to model cohesive force of detaching crack surfaces.

A.4.1. Standard Finite Element Method

In early years, people are using standard finite element method to simulate fracture problems. In standard FEM, displacement fields are interpolated by displacement at nodes multiplied by some base functions, namely shape functions, as expressed in Equation (A.29), where $\boldsymbol{u}_e$, $\boldsymbol{N}_{std}$ are nodal displacement and shape functions respectively, and $\boldsymbol{e}$ is the set that contains all standard finite elements.

$$\boldsymbol{u} = \sum_{e} \boldsymbol{u}_e \boldsymbol{N}_{std} \tag{A.29}$$

Each finite element node is associated with a space-dependent shape function N and it satisfies Kronecker delta property, which means N equals to one at corresponding node and varies linearly to zero at other node in its element patch. Note that if higher order element or higher order interpolation scheme (p-fem) is used, N does not have to vary linearly but Kronecker delta property still holds.

It can be seen that in Equation (A.29), $\boldsymbol{u}_e$ are scalers and $\boldsymbol{N}_{std}$ are spatially continuous functions so displacement field inside an FEM element is continuous. Therefore, standard FEM cannot represent discontinuity inside an element. The only way to model crack in standard FEM scheme is to put it along element edges [12], as shown in Figure A.4. During propagation process, the study domain is remeshed after each advance of crack, in order to keep crack consistent with element edges [12, 57].

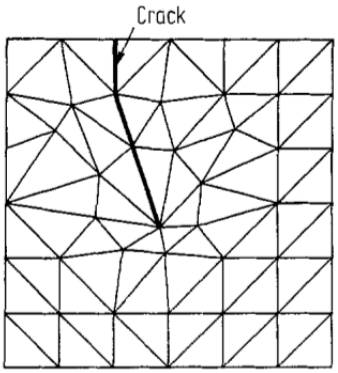

Figure A.4: Mesh of standard FEM with strong discontinuity (crack). [12]

However, standard finite element method has some drawbacks while simulating crack propagation

1. Lack of physics because it does not incorporate cohesion of surface detachment during crack opening process,

2. As remeshing is needed for each propagation step, computational cost will increase dramatically.

A.4.2. Cohesive Zone Model

In order to solve the first problem listed above, cohesive zone model (CZM) was introduced. It adds a *fracture process zone* between two crack surfaces near crack tip to model cohesive force induced by generation of new crack surfaces, as shown in Figure A.5. The cohesive force is dependent of crack opening displacement formulated by a traction-displacement relationship shown in Figure A.6. Note that the relationship can be exponential as well. When crack opening displacement is larger than a critical value, denoted by δ_u, cohesive force is released and crack is fully opened. The area under traction-displacement curve reflects energy required to form new crack surfaces, namely fracture toughness. This property gives more physical representation to cohesive zone model. Cohesive zone model is widely used in a lot of disciplines like biomechanics [58], civil structures [59] and composite materials [60]. However, CZM still cannot solve problem of mesh dependency.

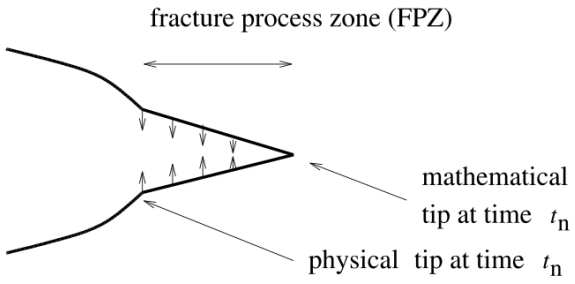

Figure A.5: Cohesive zone near crack tip. [61]

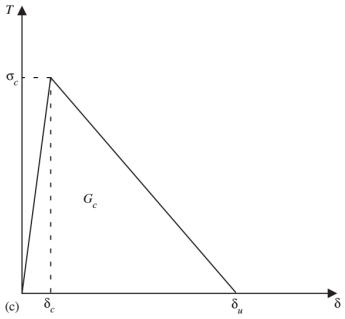

Figure A.6: Traction-displacement relationship of cohesive zone model. [58]

A.4.3. eXtended/Generalized Finite Element Method

The eXtended/Generalized Finite Element Method (X/GFEM) was proposed to tackle problem of remeshing by decoupling crack representation and background mesh [13]. This is achieved by appending additional degrees of freedom to finite element nodes, as shown in Figure A.7, where square and circle nodes represent finite element nodes with additional degrees of freedom. Associated with each degree of freedom, a discontinuous base function is added to finite element functional space. Therefore, instead of Equation (A.29), displacement interpolation formula becomes

$$\boldsymbol{u} = \sum_e \boldsymbol{u}_e \boldsymbol{N}_{std} + \sum_e \boldsymbol{N}_{std} \sum_{en} \boldsymbol{\Phi} \boldsymbol{u}_{en}. \tag{A.30}$$

Compared with Equation (A.29), the second term in Equation (A.30) is incorporated in order to represent discontinuity by discontinuous *enrichment functions* $\boldsymbol{\Phi}$. Hence, X/GFEM is able to model discontinuity inside an element. From Figure A.7, it can be observed that for a mesh of cracked domain, finite elements have three status.

1. The element is intact and does not contain any crack segments,
2. The element is fully cut by crack,
3. The element partially cut by crack and contains crack tip.

The first case is exactly the same as standard FEM so continuous shape functions are applied as in Equation (A.29). For the second case, there is a displacement jump around crack. In order to model this jump wisely, Heaviside function is defined in the local crack coordinates as enrichment function

$$H = \begin{cases} 1 & \text{at one side of crack} \\ -1 & \text{at the other side of crack} \end{cases}. \tag{A.31}$$

The third kind of element is tackled with a little bit more complicated expressions. According to theory of linear elastic fracture mechanics, the crack tip asymptotic field is expressed in terms of trigonometric functions so the enrichment strategy is

$$F(r,\theta) = \left\{ \sqrt{r}\sin\left(\frac{\theta}{2}\right), \sqrt{r}\cos\left(\frac{\theta}{2}\right), \sqrt{r}\sin\left(\frac{\theta}{2}\right)\sin(\theta), \sqrt{r}\cos\left(\frac{\theta}{2}\right)\sin(\theta) \right\}. \tag{A.32}$$

In Figure A.7, circle nodes represent nodes with Heaviside enrichment and squared nodes are enriched with Equation (A.32). If we express X/GFEM formulation in terms of enrichment strategy discussed above, Equation (A.30) becomes [13]

$$\boldsymbol{u} = \sum_{i\in I} \boldsymbol{u}_i \boldsymbol{N}_i + \sum_{j\in J} \boldsymbol{b}_j \boldsymbol{N}_j H(x) + \sum_{k\in K} \boldsymbol{N}_k (\sum_{l=1}^{4} \boldsymbol{c}_k F(r,\theta)), \tag{A.33}$$

where I, J and K are three sets corresponding to the three scenarios discussed above. u_i, b_j and c_k are degrees of freedom corresponding to I, J and K respectively.

With all aforementioned ingredients, crack can be completely decoupled from background mesh. This characteristic provides tremendous advantages because remeshing is not required during each propagation step. Instead, only additional degrees of freedom need to be appended to nodes corresponding to elements

cut by crack advance [13]. In other problems like topology optimization, where discontinuity representation is peculiar for each optimization step, mesh can be kept consistent through the whole process by X/GFEM. The convenience of X/GFEM in modeling crack propagation makes it a popular method in fracture mechanics, even available in famous commercial softwares like *Abaqus*.

X/GFEM is gaining a lot of research interest and still remains popular nowadays. People continued to propose modified versions of X/GFEM such as improved XFEM(iXFEM) [62], Corrected XFEM [25] and Stable Generalized Finite Element Method(SGFEM) [63] etc.

However, X/GFEM also suffers from some issues. Firstly, it has problem of blending element. Blending element is mixture of standard element and enriched element, where some nodes are enriched but the rest are not. Blending elements are always adjacent to cracked elements. As shown in Figure A.8, enrichment functions are nonzero in blending elements but these elements have no discontinuity. This unnecessary discontinuous enrichment could decrease convergence rate. Secondly, degrees of freedom at enriched nodes loss their physical meaning due to extra degrees of freedom appended at enriched nodes. Therefore, prescribing Dirichlet boundary condition is not as straightforward as standard FEM.

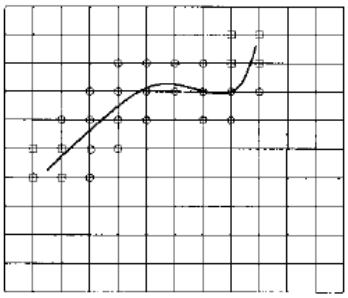

Figure A.7: X/GFEM mesh with additional degrees of freedom at finite element nodes. [13]

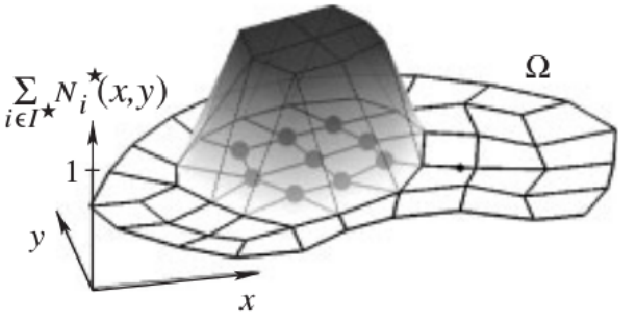

Figure A.8: N^* in this picture means N_{std} associated with enriched degrees of freedom in Equation (A.30). It is nonzero also in blending elements. [25]

A.4.4. The Discontinuity-enriched Finite Element Method

The Discontinuity-enriched Finite Element Method (DE-FEM) solves the aforementioned drawbacks of X/GFEM very well [26, 29]. The key difference between DE-FEM and X/GFEM is that the extra degrees of freedom are added inside element along discontinuity rather than at mesh nodes, as shown in Figure A.9 where red nodes denote enriched nodes and black nodes are standard nodes. The displacement interpolation is

$$\boldsymbol{u} = \sum_e \boldsymbol{u}_e \boldsymbol{N}_{std} + \sum_w \boldsymbol{u}_w \boldsymbol{\psi} + \sum_s \boldsymbol{u}_s \boldsymbol{\chi}. \tag{A.34}$$

In Equation (A.34), two terms are added compared with standard FEM formulation A.29 and they are used to model weak and strong discontinuities respectively [26, 29] with enrichment functions $\boldsymbol{\psi}$ and $\boldsymbol{\chi}$ that are constructed through standard finite element shape functions. Considering that standard FE shape functions are nonzero inside an element but zero outside this element, DE-FEM shape functions are only effective in elements that contain discontinuity, as indicated in Figure A.10, which shows a $\boldsymbol{\chi}$ in one dimensional case as an example. It can be seen that $\boldsymbol{\chi}$ incorporates a strong discontinuity and decreases linearly to zero at element nodes. $\boldsymbol{\psi}$ is similar except it replaces strong discontinuity with weak discontinuity and details can be found from work of Soghrati [29].

In fracture mechanics, at crack tip node, only weak enrichment is endowed with it whereas for other nodes along crack, they are endowed with both strong and weak enrichments. This is because for crack tip, there is no strong discontinuity (no displacement jump) and weak enrichment solely is enough to represent fields near tip.

The Discontinuity-enriched Finite Element Method preserves advantages of X/GFEM and also solves its drawbacks. Issues of blending element is fully solved by DE-FEM because enrichments $\boldsymbol{\psi}$ and $\boldsymbol{\chi}$ become zero outside cutting elements (elements cut by crack). Degrees of freedom associated with mesh nodes retain their physical meaning because $\boldsymbol{\psi}$ and $\boldsymbol{\chi}$ are zero at mesh nodes. Benefited from this characteristic, prescribing Dirichlet boundary condition is as straightforward as standard FEM. With these advantages, DE-FEM proves

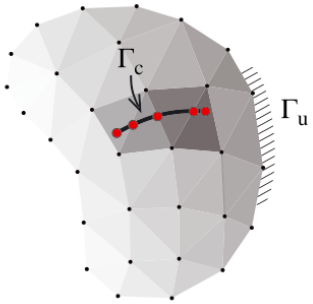

Figure A.9: DEFEM mesh with additional degrees of freedom along discontinuity. [26]

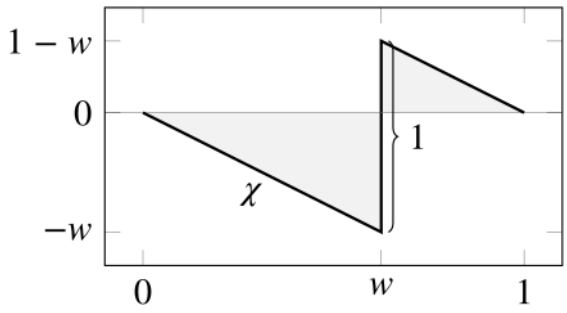

Figure A.10: DE-FEM shape function in one dimensional case. [26]

its versatility in other finite element problems like three dimensional discontinuous problems [27] and isogeometric analysis [28] etc.

B

Dynamic Crack Tip Fields

The analytical solutions of mode I and mode II crack tip fields are served as auxiliary fields of dynamic interaction integral (2.27). The detailed expressions and explanations of dynamic crack tip fields were provided following Freund [8] and Nishioka [35] in polar coordinates r and θ. For mode I crack, the displacement distribution is

$$\begin{aligned} u_x &= \frac{K_1^{dyn}}{\mu D}\sqrt{\frac{2}{\pi}}\left[\left(\alpha_2^2+1\right)\sqrt{r_1}\cos\frac{\theta_1}{2}-2\alpha_1\alpha_2\sqrt{r_2}\cos\frac{\theta_2}{2}\right] \\ u_y &= \frac{K_1^{dyn}}{\mu D}\sqrt{\frac{2}{\pi}}\left[-\alpha_1\left(\alpha_2^2+1\right)\sqrt{r_1}\sin\frac{\theta_1}{2}+2\alpha_1\sqrt{r_2}\sin\frac{\theta_2}{2}\right] \end{aligned} . \tag{B.1}$$

The stress field is

$$\begin{aligned} \sigma_{xx} &= \frac{K_1^{dyn}}{D\sqrt{2\pi}}\left[\left(\alpha_2^2+1\right)\left(2\alpha_1^2-\alpha_2^2+1\right)\frac{1}{\sqrt{r_1}}\cos\frac{\theta_1}{2}-4\alpha_1\alpha_2\frac{1}{\sqrt{r_2}}\cos\frac{\theta_2}{2}\right] \\ \sigma_{yy} &= \frac{K_1^{dyn}}{D\sqrt{2\pi}}\left[-\left(\alpha_2^2+1\right)^2\frac{1}{\sqrt{r_1}}\cos\frac{\theta_1}{2}+4\alpha_1\alpha_2\frac{1}{\sqrt{r_2}}\cos\frac{\theta_2}{2}\right] \\ \sigma_{xy} &= \frac{K_1^{dyn}}{D\sqrt{2\pi}}\left[2\alpha_1\left(\alpha_2^2+1\right)\frac{1}{\sqrt{r_1}}\sin\frac{\theta_1}{2}-2\alpha_1\left(\alpha_2^2+1\right)\frac{1}{\sqrt{r_2}}\sin\frac{\theta_2}{2}\right] \end{aligned} . \tag{B.2}$$

The spatial derivatives of displacement field are

$$\begin{aligned} \frac{\partial u_x}{\partial x} &= \frac{K_1^{dyn}B_1}{\mu\sqrt{2\pi}}\left\{\frac{1}{\sqrt{r_1}}\cos\frac{\theta_1}{2}-\frac{2\alpha_1\alpha_2}{\left(1+\alpha_2^2\right)}\frac{1}{\sqrt{r_2}}\cos\frac{\theta_2}{2}\right\} \\ \frac{\partial u_x}{\partial y} &= \frac{K_1^{dyn}B_1}{\mu\sqrt{2\pi}}\left\{\alpha_1 r_1^{-1/2}\sin\frac{\theta_1}{2}-\frac{2\alpha_1\alpha_2^2}{\left(1+\alpha_2^2\right)}r_2^{-1/2}\sin\frac{\theta_2}{2}\right\} \\ \frac{\partial u_y}{\partial x} &= \frac{K_1^{dyn}B_1}{\mu\sqrt{2\pi}}\left\{\alpha_1 r_1^{-1/2}\sin\frac{\theta_1}{2}-\frac{2\alpha_1}{\left(1+\alpha_2^2\right)}r_2^{-1/2}\sin\frac{\theta_2}{2}\right\} \\ \frac{\partial u_y}{\partial y} &= \frac{K_1^{dyn}B_1}{\mu\sqrt{2\pi}}\left\{-\alpha_1^2 r_1^{-1/2}\cos\frac{\theta_1}{2}+\frac{2\alpha_1\alpha_2}{\left(1+\alpha_2^2\right)}r_2^{-1/2}\cos\frac{\theta_2}{2}\right\} \end{aligned} . \tag{B.3}$$

For mode II crack, the displacement near crack tip is

$$\begin{aligned} u_x &= \frac{K_2^{dyn}}{\mu D}\sqrt{\frac{2}{\pi}}\left[2\alpha_2\sqrt{r_1}\sin\frac{\theta_1}{2}-\alpha_2\left(\alpha_2^2+1\right)\sqrt{r_2}\sin\frac{\theta_2}{2}\right] \\ u_y &= \frac{K_2^{dyn}}{\mu D}\sqrt{\frac{2}{\pi}}\left[2\alpha_1\alpha_2\sqrt{r_1}\cos\frac{\theta_1}{2}-\left(\alpha_2^2+1\right)\sqrt{r_2}\cos\frac{\theta_2}{2}\right] \end{aligned} . \tag{B.4}$$

The stress field for mode II dynamic crack tip is

$$\begin{aligned}
\sigma_{xx} &= \frac{K_2^{dyn}}{D\sqrt{2\pi}}\left[2\alpha_2\left(\alpha_2^2-2\alpha_1^2-1\right)\frac{1}{\sqrt{r_1}}\sin\frac{\theta_1}{2}+2\alpha_2\left(\alpha_2^2+1\right)\frac{1}{\sqrt{r_2}}\sin\frac{\theta_2}{2}\right]\\
\sigma_{yy} &= \frac{K_2^{dyn}}{D\sqrt{2\pi}}\left[2\alpha_2\left(\alpha_2^2+1\right)\frac{1}{\sqrt{r_1}}\sin\frac{\theta_1}{2}-2\alpha_2\left(\alpha_2^2+1\right)\frac{1}{\sqrt{r_2}}\sin\frac{\theta_2}{2}\right]\\
\sigma_{xy} &= \frac{K_2^{dyn}}{D\sqrt{2\pi}}\left[4\alpha_1\alpha_2\frac{1}{\sqrt{r_1}}\cos\frac{\theta_1}{2}-\left(\alpha_2^2+1\right)^2\frac{1}{\sqrt{r_2}}\cos\frac{\theta_2}{2}\right]
\end{aligned} \tag{B.5}$$

The spatial derivatives of displacement field for mode II crack tip are

$$\begin{aligned}
\frac{\partial u_x}{\partial x} &= \frac{K_2^{dyn}B_2}{\mu\sqrt{2\pi}}\left\{-r_1^{-1/2}\sin\frac{\theta_1}{2}+\frac{\left(1+\beta_2^2\right)}{2}r_2^{-1/2}\sin\frac{\theta_2}{2}\right\}\\
\frac{\partial u_x}{\partial y} &= \frac{K_2^{dyn}B_2}{\mu\sqrt{2\pi}}\left\{\beta_1 r_1^{-1/2}\cos\frac{\theta_1}{2}-\frac{\beta_2\left(1+\beta_2^2\right)}{2}r_2^{-1/2}\cos\frac{\theta_2}{2}\right\}\\
\frac{\partial u_y}{\partial x} &= \frac{K_2^{dyn}B_2}{\mu\sqrt{2\pi}}\left\{\beta_1 r_1^{-1/2}\cos\frac{\theta_1}{2}-\frac{\left(1+\beta_2^2\right)}{2\beta_2}r_2^{-1/2}\cos\frac{\theta_2}{2}\right\}\\
\frac{\partial u_y}{\partial y} &= \frac{K_2^{dyn}B_2}{\mu\sqrt{2\pi}}\left\{\beta_1^2 r_1^{-1/2}\sin\frac{\theta_1}{2}-\frac{\left(1+\beta_2^2\right)}{2}r_2^{-1/2}\sin\frac{\theta_2}{2}\right\}
\end{aligned} \tag{B.6}$$

In the aforementioned formulas, the field parameters are all defined by polar coordinates r, θ and dilatational and shear wave speeds c_1, c_2 as well as crack propagation speed v.

$$\alpha_1 = \sqrt{1-\frac{v^2}{c_1^2}}, \qquad \alpha_2 = \sqrt{1-\frac{v^2}{c_2^2}}. \tag{B.7}$$

The rest of coordinate parameters are

$$r1 = r\sqrt{1-\left(\frac{v\sin(\theta)}{c_1}\right)^2}, \qquad r2 = r\sqrt{1-\left(\frac{v\sin(\theta)}{c_2}\right)^2}. \tag{B.8}$$

θ_1 and θ_2 are in the same quadrant as θ satisfying

$$\tan(\theta_1) = \alpha_1\tan(\theta), \qquad \tan(\theta_2) = \alpha_2\tan(\theta). \tag{B.9}$$

Other parameters are

$$D(v) = 4\alpha_1\alpha_2 - (1+\alpha_2^2)^2, \tag{B.10}$$

$$B_1 = \frac{1+\alpha_2^2}{D}, \qquad B_2 = \frac{2\alpha_2}{D}. \tag{B.11}$$

C

Newmark Method and Bathe's Method

In this appendix, more details of Newmark and Bathe's method are elaborated. Also, a comparison between them will be made by a benchmark example.

C.1. Other forms of Newmark implementation

Besides *d-form*, Newmark type methods can also be implemented in velocity form (v-form) and acceleration form (a-form) [32].

v-form

The governing equation is

$$\begin{aligned} \Delta \boldsymbol{F} &= \boldsymbol{F}_{n+1}^{ext} - \boldsymbol{M}\ddot{\boldsymbol{u}}_{n+1}^{i} - \boldsymbol{K}\boldsymbol{u}_{n+1}^{i} \\ \boldsymbol{C}^{*} &= \frac{1}{\Delta t\gamma}\boldsymbol{M} + \frac{\Delta t\beta}{\gamma}\boldsymbol{K} \\ \boldsymbol{C}^{*}\Delta\dot{\boldsymbol{u}} &= \Delta \boldsymbol{F} \end{aligned} \tag{C.1}$$

And the iterative process is

$$\begin{aligned} \dot{\boldsymbol{u}}_{n+1}^{i+1} &= \dot{\boldsymbol{u}}_{n+1}^{i} + \Delta\dot{\boldsymbol{u}} \\ \ddot{\boldsymbol{u}}_{n+1}^{i+1} &= \left(\dot{\boldsymbol{u}}_{n+1}^{i+1} - \tilde{\dot{\boldsymbol{u}}}_{n+1}\right)/(\Delta t\gamma) \\ \boldsymbol{u}_{n+1}^{i+1} &= \tilde{\boldsymbol{u}}_{n+1} + \Delta t^{2}\beta\ddot{\boldsymbol{u}}_{n+1}^{i+1} \end{aligned} \tag{C.2}$$

a-form

The governing equation is

$$\begin{aligned} \Delta \boldsymbol{F} &= \boldsymbol{F}_{n+1}^{ext} - \boldsymbol{M}\ddot{\boldsymbol{u}}_{n+1}^{i} - \boldsymbol{K}\boldsymbol{u}_{n+1}^{i} \\ \boldsymbol{M}^{*} &= \boldsymbol{M} + \Delta t^{2}\beta\boldsymbol{K} \\ \boldsymbol{M}^{*}\Delta\ddot{\boldsymbol{u}} &= \Delta \boldsymbol{F} \end{aligned} \tag{C.3}$$

And the iterative process is

$$\begin{aligned} \ddot{\boldsymbol{u}}_{n+1}^{i+1} &= \ddot{\boldsymbol{u}}_{n+1}^{i} + \Delta\ddot{\boldsymbol{u}} \\ \dot{\boldsymbol{u}}_{n+1}^{i+1} &= \tilde{\dot{\boldsymbol{u}}}_{n+1} + \Delta t\gamma\ddot{\boldsymbol{u}}_{n+1}^{i+1} \\ \boldsymbol{u}_{n+1}^{i+1} &= \tilde{\boldsymbol{u}}_{n+1} + \Delta t^{2}\beta\ddot{\boldsymbol{u}}_{n+1}^{i+1} \end{aligned} \tag{C.4}$$

C.2. A Comparison between Newmark and Bathe's Method

The functionalities of Newmark constant acceleration method and Bathe's method are compared by a cantilever beam free vibration problem in this section. The advantages of Bathe method over Newmark is addressed.

Consider a cantilever beam as shown in Figure C.1 with left end fixed and the rest of boundary free. The initial condition is given to its neutral line such that it vibrates freely with its first eigenmode. The analytical

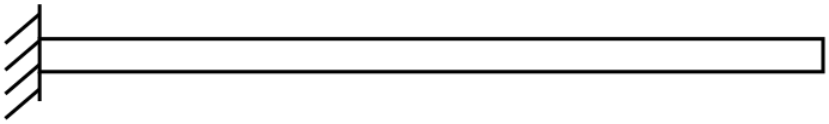

Figure C.1: Illustration of a cantilever beam.

solution of displacement , velocity and acceleration of right end point on neutral line is

$$d = d_m \left(\cosh(\lambda x) - \cos(\lambda x) - \frac{\cosh(\lambda L) + \cos(\lambda L)}{\sinh(\lambda L) + \sin(\lambda L)} (\sinh(\lambda L) - \sin(\lambda L)) \right) \cos(\omega t) \tag{C.5}$$

$$v = v_m \left(\cosh(\lambda x) - \cos(\lambda x) - \frac{\cosh(\lambda L) + \cos(\lambda L)}{\sinh(\lambda L) + \sin(\lambda L)} (\sinh(\lambda L) - \sin(\lambda L)) \right) (-\omega \sin(\omega t)) \tag{C.6}$$

$$a = a_m \left(\cosh(\lambda x) - \cos(\lambda x) - \frac{\cosh(\lambda L) + \cos(\lambda L)}{\sinh(\lambda L) + \sin(\lambda L)} (\sinh(\lambda L) - \sin(\lambda L)) \right) \left(-\omega^2 \cos(\omega t) \right) \tag{C.7}$$

where d_m, v_m and a_m are parameters defined by vibration amplitude. L is length of the cantilever beam and ω is its first eigenfrequency. x is Cartesian coordinate. λ in this case is $1.8571/L$.

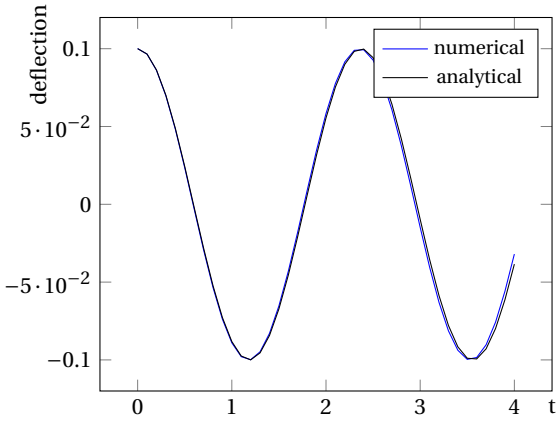

Figure C.2: Displacement computed by trapezoidal rule.

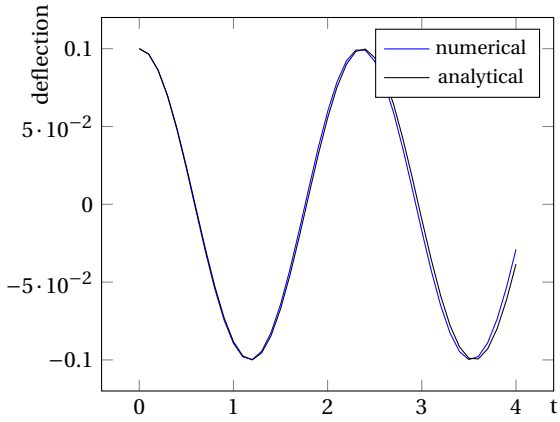

Figure C.3: Displacement computed by Bathe's method.

Figure C.2 to C.7 compare displacement, velocity and acceleration of point at free end along neutral line. It can be seen that both Newmark trapezoidal rule and Bathe's method predict displacement and velocity very well. However, when it comes to acceleration, Newmark trapezoidal rule fails to converge and oscillates with large amplitude. Bathe's method still converges except the first few steps. This result is the same as what Bathe got in their paper [33].

From Figure C.3 and Figure C.5, it can be observed Bathe's method provides slightly larger frequency than Newmark trapezoidal rule and thus will cause phase shift after long simulation time. In this thesis, this slight increase of frequency will not influence result because we are more interested in crack path than propagation at each time instance. Therefore, from all these results, we can conclude that Bathe's method is a good alternative to get better simulation results when Newmark type methods fail.

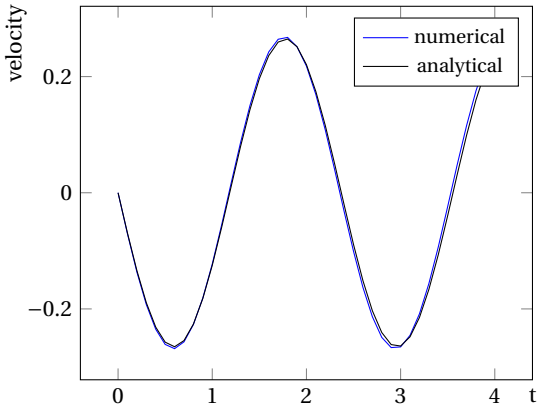

Figure C.4: Velocity computed by trapezoidal rule.

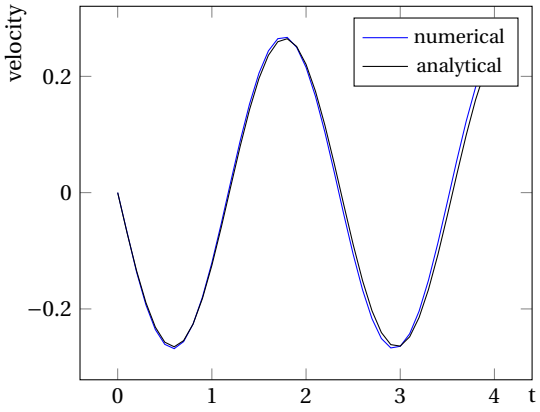

Figure C.5: Velocity computed by Bathe's method.

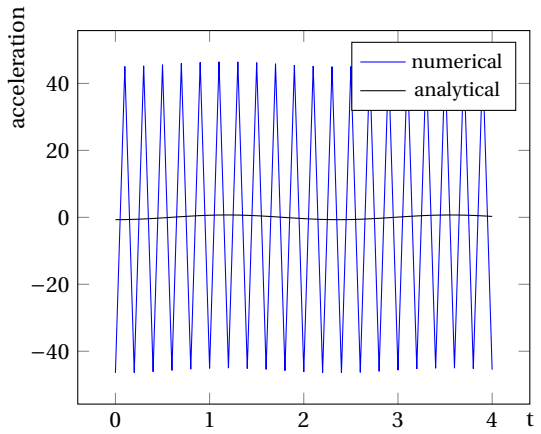

Figure C.6: Acceleration computed by trapezoidal rule.

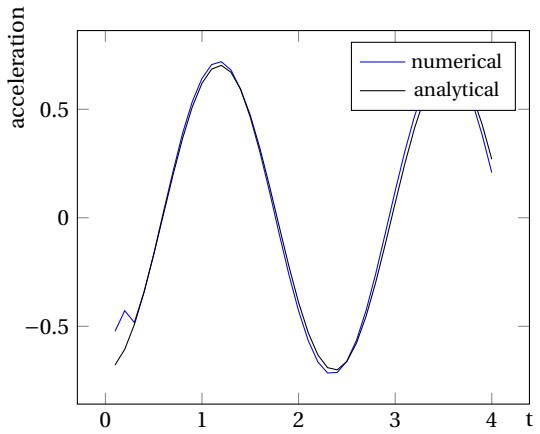

Figure C.7: Acceleration computed by Bathe's method.

D

Working with *Hybrida* Geometric Engine

Hybrida is our in-house finite element library and it has a very powerful geometric engine which deals with interaction of mesh and discontinuity, including parent and integration elements. A tricky question for crack propagation is how to get new mesh topology after each step of advance. This is achieved by *Hybrida* geometric engine which already has functions to create crack segments. In order to make best use of these functions, the new crack segment is firstly modeled as another crack and then merged with original crack as propagated segment. The algorithm is summarized as Figure D.1 and follows.

1. The crack before propagation is shown in Figure D.1a. Coordinates of new crack tip after propagation is computed by equation (2.32) to equation (2.34), as shown in Figure D.1b.
2. Then a point near old tip along propagation direction is picked. Take this point and the new crack tip together to form a new crack segment. This process can be done directly by existing functions in *Hybrida* geometric engine, as shown in Figure D.1c. At this phase, all parent elements are partitioned into integration elements.
3. Merge the point close to old crack tip with old crack tip and re-partition the parent element corresponding to these nodes, as shown in Figure D.1d. By this phase a propagated segment is created.

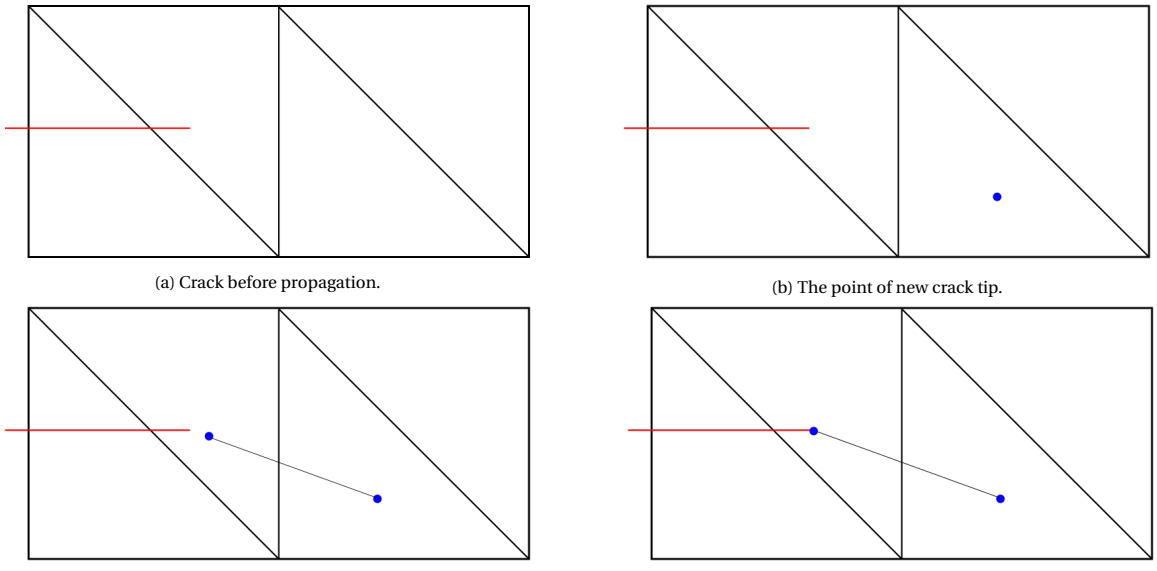

(a) Crack before propagation.

(b) The point of new crack tip.

(c) Create new crack segment.

(d) Merge the new crack segment with old crack tip.

Figure D.1: Process of propagating a crack with *Hybrida* geometric engine.

E

Some Additional Simulation Results

In this appendix, some additional simulation results of numerical examples in Section 2.6 are shown.

E.1. Mode I stationary Crack with Dynamic Loading

In this section, stress distributions of example in Section 2.6.1 by Newmark constant acceleration method and Bathe's method are compared. Figure E.1 and Figure E.2 show vertical stress distributions σ_{yy} at time $t = 0.00027s$, $t = 0.00054s$ and $t = 0.00081s$. Compared Figure E.1 with Figure E.2, it can be seen that both Newmark constant acceleration method and Bathe's method result in similar stress distribution. In Figure E.2, stress wave is smooth rather than showing unrealistic 'wave pattern' as shown in Figure E.1. This is because Bathe's method has better capability for removing spurious oscillations.

Process of stress waves propagation can be summarized as follows

- When time $t > 0$, a vertical distributed load is applied on top edge of structure, which generates a dilatational wave. This dilatational wave propagates through upper half of structure vertically as shown in Figure E.2a, until time $t = 0.000324s$ it reaches the crack.
- At $t = 0.000324s$ right half of stress wave propagates through its original vertical direction whereas the left half is reflected by crack surface. The crack surface reflects a dilatational stress wave and the crack tip reflects both dilatational and shear stress wave [8]. Shear stress wave propagates slower than dilatational wave.
- The two halves of stress wave propagates upward and downward as shown in Figure E.2b until they reach top and bottom edge, respectively, at time $t = 0.000666s$ then they are reflected by boundary and reverse their directions.
- Finally the simulations end at time $t = 0.0009s$ at which the stress waves are traveling downwards (left half) and upwards (right half), respectively.

E.2. A First Glance into Dynamic Crack Propagation

In Section 2.6.3, a 115×65 mesh was used. However, it could be further proved that increasing number of elements will not mitigate this kind of oscillations. The result with mesh 165×85 is shown in Figure E.3. Compared it with Figure 2.12, it can be seen that level of oscillations is similar so increasing number of elements does not result in better accuracy. Therefore, the oscillations are mesh independent.

(a) At time $t = 0.00027s$.

(b) At time $t = 0.00054s$.

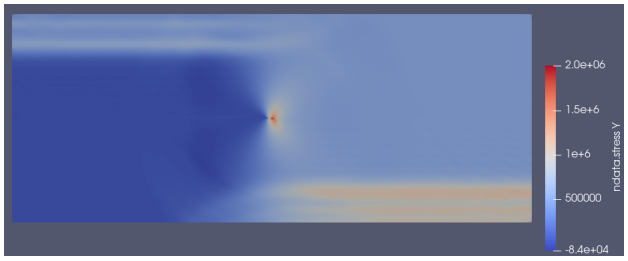

(c) At time $t = 0.00081s$.

Figure E.1: σ_{yy} distribution by Newmark trapezoidal rule.

(a) At time $t = 0.00027s$.

(b) At time $t = 0.00054s$.

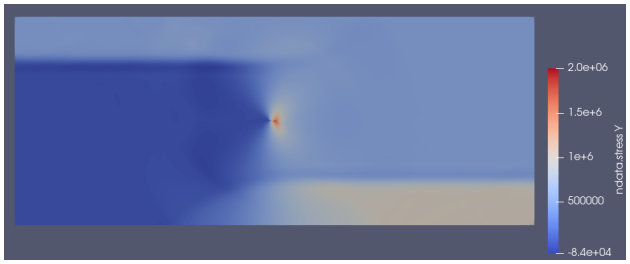

(c) At time $t = 0.00081s$.

Figure E.2: σ_{yy} distribution by Bathe's method.

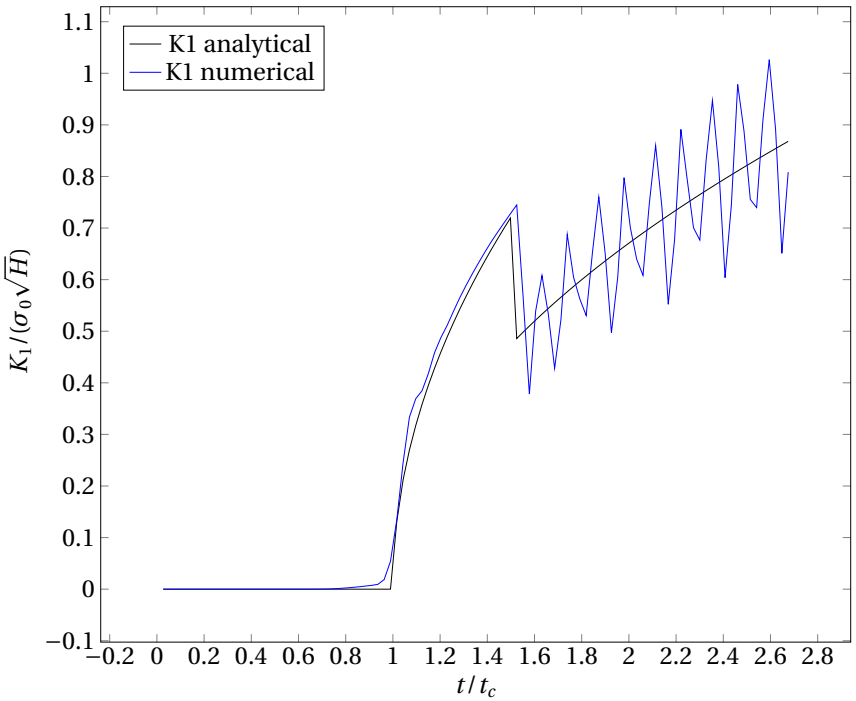

Figure E.3: Numerical result for example 2.6.3 with fine mesh of 165 × 85.

Bibliography

[1] A. Kobayashi and N. Ohtani. “Dynamic Fracture in Aerospace High Polymers”. In: vol. 132. ACS Symposium Series. 0. AMERICAN CHEMICAL SOCIETY, 1980, pp. 367–377.

[2] T.-T. Nguyen, M. Weiler, and D. Waldmann. “Experimental and numerical analysis of early age behavior in non-reinforced concrete”. In: *Construction and Building Materials* 210 (2019), pp. 499–513.

[3] H. Peterlik, P. Roschger, K. Klaushofer, and P. Fratzl. “From brittle to ductile fracture of bone”. In: *Nature Materials* 5.1 (Jan. 2006), pp. 52–55.

[4] S. Yakovleva, I. Buslaeva, S. Makharova, and A. Levin. “Damage, brittle fracture resistance and working capacity of a KAMAZ vehicle leaf spring when operating in the North”. In: *Procedia Structural Integrity* 20 (2019). 1st International Conference on Integrity and Lifetime in Extreme Environment (ILEE-2019), pp. 154–160.

[5] R. P. Reed, B. M. Institute., and U. States. *The Economic effects of fracture in the United States*. Special publication ;647-1, 647-2. pt. 1. A synopsis of the September 30, 1982 report to NBS by Battelle Columbus Laboratories / R.P. Reed, J.H. Smith, B.W. Christ–pt. 2. A report to NBS by Batelle Columbus Laboratories / JJ Duga ... [et al.]. Washington, D.C.: U.S. Dept. of Commerce, National Bureau of Standards, 1983, p. 2 v.

[6] A. J. Rosakis. “Analysis of the optical method of caustics for dynamic crack propagation”. In: *Engineering Fracture Mechanics* 13.2 (1980), pp. 331–347.

[7] W. Wu and C. Ni. “Probabilistic models of fatigue crack propagation and their experimental verification”. In: *Probabilistic Engineering Mechanics* 19.3 (2004). Fifth International Conference on Stochastic Structural Dynamics, pp. 247–257.

[8] L. B. Freund. *Dynamic Fracture Mechanics*. Cambridge Monographs on Mechanics. Cambridge University Press, 1990.

[9] B. Lawn. *Fracture of Brittle Solids*. 2nd ed. Cambridge Solid State Science Series. Cambridge University Press, 1993.

[10] X.-P. Xu and A. Needleman. “Numerical simulations of fast crack growth in brittle solids”. In: *Journal of the Mechanics and Physics of Solids* 42.9 (1994), pp. 1397–1434.

[11] S. N. Atluri and T. Nishioka. “Numerical studies in dynamic fracture mechanics”. In: *International Journal of Fracture* 27.3 (Mar. 1985), pp. 245–261.

[12] D. V. Swenson and A. R. Ingraffea. “Modeling mixed-mode dynamic crack propagation nsing finite elements: Theory and applications”. In: *Computational Mechanics* 3.6 (Sept. 1988), pp. 381–397.

[13] N. Moës, J. Dolbow, and T. Belytschko. “A finite element method for crack growth without remeshing”. In: *International Journal for Numerical Methods in Engineering* 46.1 (1999), pp. 131–150.

[14] T. Belytschko, H. Chen, J. Xu, and G. Zi. “Dynamic crack propagation based on loss of hyperbolicity and a new discontinuous enrichment”. In: *International Journal for Numerical Methods in Engineering* 58.12 (2003), pp. 1873–1905.

[15] C. Duarte, O. Hamzeh, T. Liszka, and W. Tworzydlo. “A generalized finite element method for the simulation of three-dimensional dynamic crack propagation”. In: *Computer Methods in Applied Mechanics and Engineering* 190.15 (2001), pp. 2227–2262.

[16] T. Belytschko and H. Chen. “Singular Enrichment Finite Element Method for Elastodynamic Crack Propagation”. In: *International Journal of Computational Methods* 01.01 (2004), pp. 1–15.

[17] J.-H. Song, P. M. A. Areias, and T. Belytschko. “A method for dynamic crack and shear band propagation with phantom nodes”. In: *International Journal for Numerical Methods in Engineering* 67.6 (2006), pp. 868–893.

[18] M. Attigui and C. Petit. “Mixed-mode separation in dynamic fracture mechanics: New path independent integrals”. In: *International Journal of Fracture* 84.1 (Mar. 1997), pp. 19–36.

[19] J. Réthoré, A. Gravouil, and A. Combescure. “An energy-conserving scheme for dynamic crack growth using the eXtended finite element method”. In: *International Journal for Numerical Methods in Engineering* 63.5 (2005), pp. 631–659.

[20] T. Menouillard, J. Réthoré, A. Combescure, and H. Bung. “Efficient explicit time stepping for the eXtended Finite Element Method (X-FEM)”. In: *International Journal for Numerical Methods in Engineering* 68.9 (2006), pp. 911–939.

[21] T. Menouillard, J.-H. Song, Q. Duan, and T. Belytschko. “Time dependent crack tip enrichment for dynamic crack propagation”. In: *International Journal of Fracture* 162.1 (Mar. 2010), pp. 33–49.

[22] L. Wen and R. Tian. “Improved XFEM: Accurate and robust dynamic crack growth simulation”. In: *Computer Methods in Applied Mechanics and Engineering* 308 (2016), pp. 256–285.

[23] T. Menouillard and T. Belytschko. “Smoothed nodal forces for improved dynamic crack propagation modeling in XFEM”. In: *International Journal for Numerical Methods in Engineering* 84.1 (2010), pp. 47–72.

[24] Z. L. Liu, T. Menouillard, and T. Belytschko. “An XFEM/Spectral element method for dynamic crack propagation”. In: *International Journal of Fracture* 169.2 (June 2011), pp. 183–198.

[25] T.-P. Fries. “A corrected XFEM approximation without problems in blending elements”. In: *International Journal for Numerical Methods in Engineering* 75.5 (2008), pp. 503–532.

[26] A. M. Aragón and A. Simone. “The Discontinuity-Enriched Finite Element Method”. In: *International Journal for Numerical Methods in Engineering* 112.11 (2017), pp. 1589–1613.

[27] J. Zhang, S. J. van den Boom, F. van Keulen, and A. M. Aragón. “A stable discontinuity-enriched finite element method for 3-D problems containing weak and strong discontinuities”. In: *Computer Methods in Applied Mechanics and Engineering* 355 (2019), pp. 1097–1123.

[28] E. De Lazzari, S. J. van den Boom, J. Zhang, F. van Keulen, and A. M. Aragón. “A critical view on the use of NURBS to improve geometry representation in enriched finite element methods”. In: *International Journal for Numerical Methods in Engineering* ().

[29] S. Soghrati, A. M. Aragón, C. Armando Duarte, and P. H. Geubelle. “An interface-enriched generalized FEM for problems with discontinuous gradient fields”. In: *International Journal for Numerical Methods in Engineering* 89.8 (2012), pp. 991–1008.

[30] N. M. Newmark. “A Method of Computation for Structural Dynamics”. In: *ASCE Journal of the Engineering Mechanics Division* 85 (1959), pp. 67–94.

[31] T. J. R. Hughes. *The Finite Element Method: Linear Static and Dynamic Finite Element Analysis*. New Jersey: Prentice-Hall, 1987.

[32] T. J. Hughes, K. S. Pister, and R. L. Taylor. “Implicit-explicit finite elements in nonlinear transient analysis”. In: *Computer Methods in Applied Mechanics and Engineering* 17-18 (1979), pp. 159–182.

[33] K.-J. Bathe and G. Noh. “Insight into an implicit time integration scheme for structural dynamics”. In: *Computers & Structures* 98-99 (2012), pp. 1–6.

[34] K.-J. Bathe. “Conserving energy and momentum in nonlinear dynamics: A simple implicit time integration scheme”. In: *Computers & Structures* 85.7 (2007), pp. 437–445.

[35] T. Nishioka and S. Atluri. “Path-independent integrals, energy release rates, and general solutions of near-tip fields in mixed-mode dynamic fracture mechanics”. In: *Engineering Fracture Mechanics* 18.1 (1983), pp. 1–22.

[36] A. A. Griffith and G. I. Taylor. “VI. The phenomena of rupture and flow in solids”. In: *Philosophical Transactions of the Royal Society of London. Series A, Containing Papers of a Mathematical or Physical Character* 221.582-593 (1921), pp. 163–198.

[37] G. R. Irwin. “Onset of Fast Crack Propagation in High Strength Steel and Aluminum Alloys”. In: *Sagamore Research Conference Proceeding* (1956).

[38] H. Cheng and X. Zhou. “A multi-dimensional space method for dynamic cracks problems using implicit time scheme in the framework of the extended finite element method”. In: *International Journal of Damage Mechanics* 24.6 (2015), pp. 859–890.

[39] D. Xu, Z. Liu, X. Liu, Q. Zeng, and Z. Zhuang. “Modeling of dynamic crack branching by enhanced extended finite element method”. In: *Computational Mechanics* 54.2 (Aug. 2014), pp. 489–502.

[40] A. Idesman, A. Bhuiyan, and J. Foley. “Accurate finite element simulation of stresses for stationary dynamic cracks under impact loading”. In: *Finite Elements in Analysis and Design* 126 (2017), pp. 26–38.

[41] Y. J. Lee and L. B. Freund. “Fracture Initiation Due to Asymmetric Impact Loading of an Edge Cracked Plate”. In: *Journal of Applied Mechanics* 57.1 (Mar. 1990), pp. 104–111.

[42] T. Menouillard and T. Belytschko. “Dynamic fracture with meshfree enriched XFEM”. In: *Acta Mechanica* 213.1 (Aug. 2010), pp. 53–69.

[43] J. F. Kalthoff. “Modes of dynamic shear failure in solids”. In: *International Journal of Fracture* 101.1 (Jan. 2000), pp. 1–31.

[44] J.-H. Song and T. Belytschko. “Cracking node method for dynamic fracture with finite elements”. In: *International Journal for Numerical Methods in Engineering* 77.3 (2009), pp. 360–385.

[45] T.L.Anderson. *Fracture Mechanics : Fundamentals and Applications*. Cambridge, United Kingdom: Cambridge University Press, 2015.

[46] D. Broek. “The elastic crack-tip stress field”. In: *Elementary engineering fracture mechanics*. Dordrecht: Springer Netherlands, 1982, pp. 67–90.

[47] Rice:1968. “A Path Independent Integral and the Approximate Analysis of Strain Concentration by Notches and Cracks”. In: *Journal of Applied Mechanics* 35.2 (June 1968), pp. 379–386.

[48] F. Erdogan and G. C. Sih. “On the Crack Extension in Plates Under Plane Loading and Transverse Shear”. In: *Journal of Basic Engineering* 85.4 (Dec. 1963), pp. 519–525.

[49] S. K. Maiti and R. A. Smith. “Comparison of the criteria for mixed mode brittle fracture based on the preinstability stress-strain field”. In: *International Journal of Fracture* 24.1 (1984), pp. 5–22.

[50] A. T. Zehnder. *Fracture Mechanics*. Lecture Notes in Applied and Computational Mechanics. The Netherlands: Springer, Dordrecht, 2012.

[51] W. M. Telford, L. P. Geldart, and R. E. Sheriff. *Applied Geophysics*. 2nd ed. Cambridge University Press, 1990.

[52] F. F. Abraham and H. Gao. “How Fast Can Cracks Propagate?” In: *Phys. Rev. Lett.* 84 (14 Apr. 2000), pp. 3113–3116.

[53] C.-H. Chen, E. Bouchbinder, and A. Karma. “Instability in dynamic fracture and the failure of the classical theory of cracks”. In: *Nature Physics* 13.12 (Dec. 2017), pp. 1186–1190.

[54] I. Procaccia and J. Zylberg. “Propagation mechanism of brittle cracks”. In: *Phys. Rev. E* 87 (1 Jan. 2013), p. 012801.

[55] M. Adda-Bedia. “Brittle fracture dynamics with arbitrary paths III. The branching instability under general loading”. In: *Journal of the Mechanics and Physics of Solids* 53.1 (2005), pp. 227–248.

[56] E. H. Y. Ph.D. “LXXV. The moving griffith crack”. In: *The London, Edinburgh, and Dublin Philosophical Magazine and Journal of Science* 42.330 (1951), pp. 739–750.

[57] P. Wawrzynek and A. Ingraffea. “Interactive finite element analysis of fracture processes: An integrated approach”. In: *Theoretical and Applied Fracture Mechanics* 8.2 (1987), pp. 137–150.

[58] A. Ural and D. Vashishth. “Cohesive finite element modeling of age-related toughness loss in human cortical bone”. In: *Journal of Biomechanics* 39.16 (2006), pp. 2974–2982.

[59] A. Hillerborg, M. Modéer, and P.-E. Petersson. “Analysis of crack formation and crack growth in concrete by means of fracture mechanics and finite elements”. In: *Cement and Concrete Research* 6.6 (1976), pp. 773–781.

[60] S. A. Ponnusami, S. Turteltaub, and S. van der Zwaag. “Cohesive-zone modelling of crack nucleation and propagation in particulate composites”. In: *Engineering Fracture Mechanics* 149 (2015), pp. 170–190.

[61] N. Moës and T. Belytschko. “Extended finite element method for cohesive crack growth”. In: *Engineering Fracture Mechanics* 69.7 (2002), pp. 813–833.

[62] R. Tian and L. Wen. “Improved XFEM—An extra-dof free, well-conditioning, and interpolating XFEM”. In: *Computer Methods in Applied Mechanics and Engineering* 285 (2015), pp. 639–658.

[63] I. Babuška and U. Banerjee. “Stable Generalized Finite Element Method (SGFEM)”. In: *Computer Methods in Applied Mechanics and Engineering* 201-204 (2012), pp. 91–111.